JPRS-CST-91-014
24 JUNE 1991

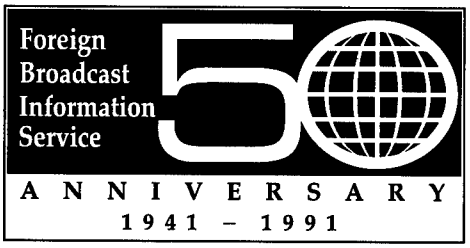

JPRS Report

Science & Technology

China

JPRS-CST-91-014
24 JUNE 1991

SCIENCE & TECHNOLOGY

CHINA

CONTENTS

Research, Design of SG-1 Free Electron Laser

91FE0192A Chengdu QIANG JIGUANG YU LIZI SHU [HIGH-POWER LASER AND PARTICLE BEAMS] in Chinese Vol 2 No 3, Aug 90 pp 257-272 [MS received 29 Jun 90]

[Article by Hui Zhongxi [1920 6988 6932] of the China Academy of Engineering Physics: "Research, Design of Shuguang-1 Free Electron Laser"]

[Text] Abstract

The Shuguang-1 (SG-1) is a high-power millimeter-wave-band free electron laser (FEL). It consists of a 3.5 MeV induction linear accelerator (linac), electron-beam (e-beam) modulation system, variable wiggler and microwave source. The physical design and major technical parameters are described in this paper. Furthermore, experimental research on major components, computer simulation and special features associated with the physical design and structure is also analyzed.

I. Introduction

The FEL is a new type of high-power laser. It is based on a different mechanism to generate coherent light compared to other lasers. It is a device which converts the kinetic energy of a relativistic e-beam in vacuum into coherent electromagnetic radiation through interaction with a pumping field (periodic magnetic field or electromagnetic field). It can operate as an oscillator as well as an amplifier. In essence, it is analogous to a traveling-wave-tube oscillator or traveling-wave-tube amplifier. Under the influence of the pumping field, electrons in the wiggler produce a periodic radial motion. The radiation wave field interacts with the transverse component of the motion of the electrons to generate an axial non-linear pondero-motive force. This force exerted on electrons creates longitudinal bunching and electron bunching amplifies the coherent radiation wave. More precisely, electrons with energy slightly higher than the resonance energy will perform work on the gradually increasing pondero-motive wave and the radiation field intensifies. On the other hand, electrons with energy less than the resonance energy will absorb energy from the pondero-motive wave to weaken the radiation field. Therefore, by changing the resonance energy, an FEL may become a laser amplifier or a laser accelerator.

The SG-1 FEL is a high-power 8.6-mm FEL amplifier. It consists of a linac (including injector, acceleration elements, Marx generator, pulse formation line, etc.), e-beam modulation system (including energy-dispersion selector, emission selector, quadrupole magnetic lens, etc.), variable wiggler, microwave seed source, control system and diagnostic system. Figure 1 shows its block diagram. The overall layout is shown in Figure 2.

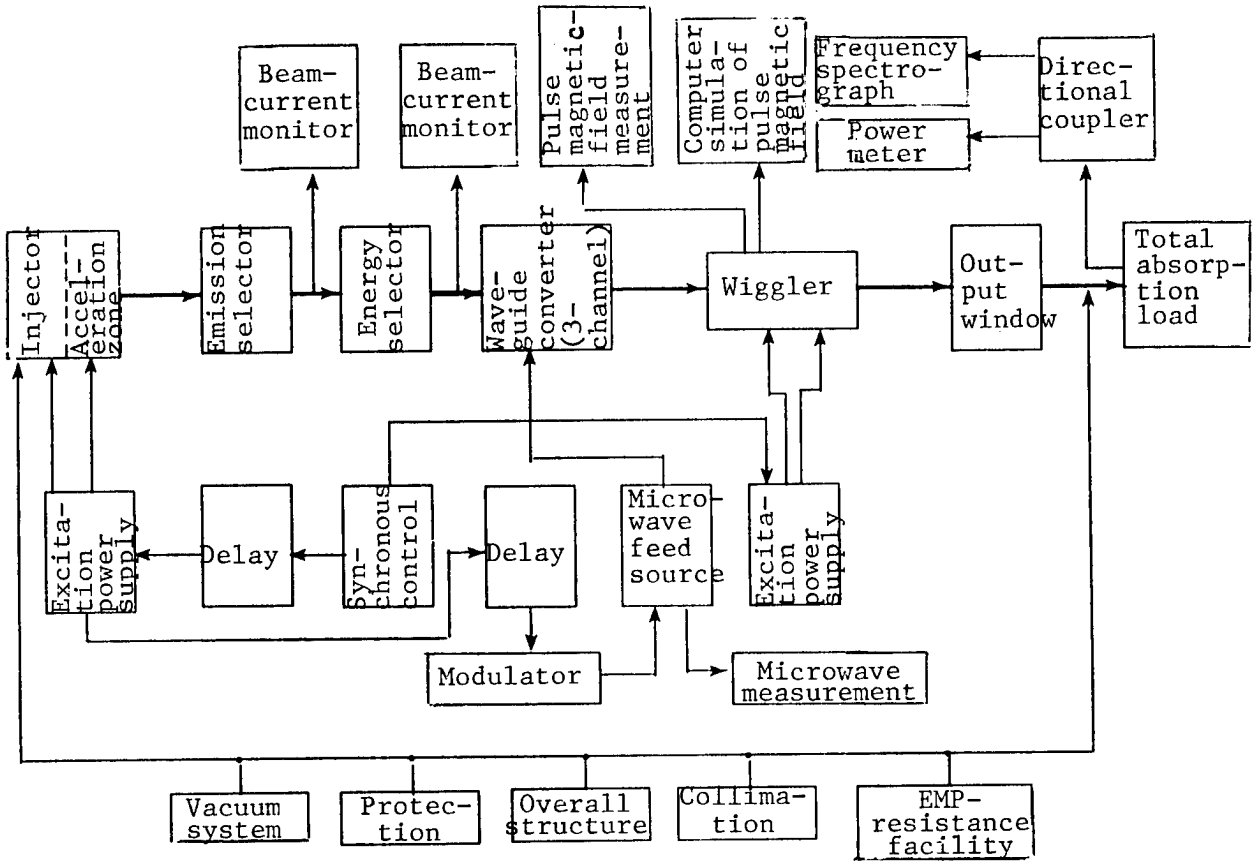

Figure 1. Block Diagram of the SG-1 FEL Amplifier

Increasing energy conversion efficiency and power output is an important aspect of FEL research. To this end, it is necessary to study how to increase the e-beam current, improve beam quality, control beam transport technology, prevent beam blowup (BBU effect), analyze physical problems associated with the energy-conversion process, master the physical and engineering design of high-efficiency wigglers, and study other FEL-related problems such as the photoconductivity effect. The purpose of developing the SG-1 FEL is to conduct studies on these physical and technical issues. Through theoretical analysis, numerical simulation and experimental study, the adequacy of the physical design and the accuracy of the numerical program can be verified. Furthermore, qualitative rules and design-optimization methods can be obtained.

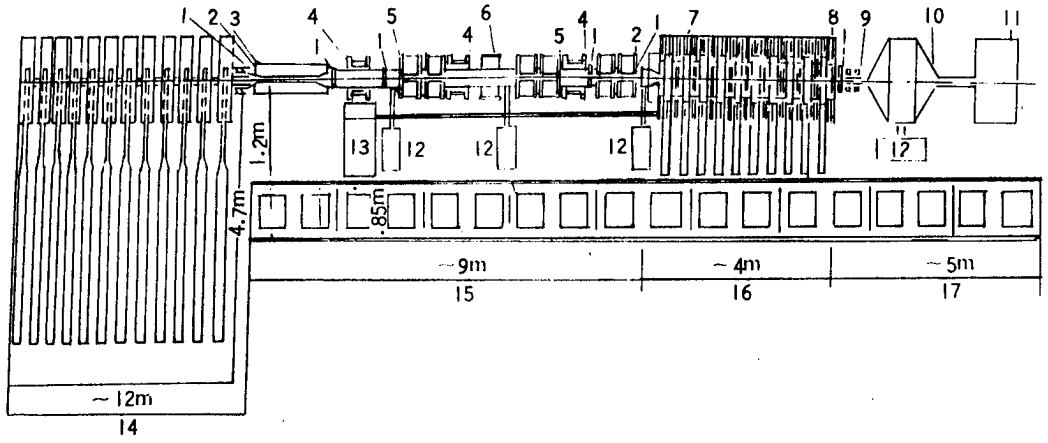

Figure 2. Layout of the Experimental SG-1 FEL Amplifier

1 -- observation hole, 2 -- bellows, 3 -- emission selector, 4 -- regulating magnet, 5 -- quadrupole pair, 6 -- energy selector, 7 -- electron-microwave synthesizer, 8 -- wiggler, 9 -- bending magnet, 10 -- load box, 11 -- test equipment, 12 -- vacuum equipment, 13 -- input microwave source, 14 -- accelerator area, 15 -- e-beam modulation zone, 16 -- FEL active zone, 17 -- diagnostic zone

II. Theoretical Design and Analysis of the SG-1 FEL Amplifier

Theoretical analysis and numerical simulation of the SG-1 FEL amplifier are done with the WAGFEL program.[1] The program was written based on the KMR single-particle theory[2] using the same concept as the FRED program. Three-dimensional electron motion is considered. Averaging is done to the fast and slow portion in a wiggler cycle. The slowing motion is described by the Betatron equation of motion. The program takes into consideration the effects of space charge, the waveguide and the fact that the axial speed of the electrons is lower than the speed of light. In the TE_{01} mode, the equation of electron state in the FEL can be summarized as follows:

$$\frac{d\gamma_i}{dz} = -\frac{a_w(r_i)\,e_s(r_i)}{\beta_{\parallel}\,\gamma_i} f_B \sin\psi_i - \frac{16\pi e}{m_0 c^3 \beta_{\parallel}} \sum_{m=1}^{s} J_0(m\zeta)\,\frac{1}{m(k_s+k_w)}\,\frac{1}{N\pi r_b^2}$$

$$\cdot\,[1-\frac{r_i^2}{r_b^2}-\frac{4}{m^2 g^2 r_b^2}+f_B I_0(mgr_i)]\,[\langle\sin m\theta_i\rangle\cos m\theta_i-\langle\cos m\theta_i\rangle\sin m\theta_i] \qquad (1)$$

$$\frac{d\theta_i}{dz} = k_w+\delta k_s-\frac{\omega_p}{\gamma_i c}-\frac{\omega_s}{\beta_{\parallel}(1+\beta_{\parallel})c\gamma_i^2}\,[1+a_w^2(r_i)+a_s^2(r_i)$$

$$-2a_w(r_i)\,a_s(r_i)f_B\cos\psi_i+\gamma_i^2\beta_{\perp i}^2] \qquad (2)$$

$$\frac{dx_i}{dz}+k_{Bx}^2 x_i=0 \qquad (3)$$

$$\frac{dy_i}{dz^2}+k_{By}^2 y_i=0 \cdot \qquad (4)$$

$$\frac{de_s}{dz} = \frac{\omega_s}{k_s} \frac{4\pi e}{m_0 c^4} \left(\frac{I}{abN} \right) \sum_{i=1}^{N} a_w(r_i) f_B \cos\left(\frac{\pi}{b} y_i \right) \frac{\sin\psi_i}{\gamma_i} \qquad (5)$$

$$e_s \frac{d\varphi_s}{dz} = \frac{\omega_s}{k_s} \frac{4\pi e}{m_0 c^4} \left(\frac{I}{abN} \right) \sum_{i=1}^{N} a_w(r_i) f_B \cos\left(\frac{\pi}{b} y_i \right) \frac{\cos\psi_i}{\gamma_i} \qquad (6)$$

where $\theta_i = \psi_i - \varphi_s$, φ_s is the slowing phase of the optical field, ψ_i is the phase of the ith electron in the pondero-motive potential well, $\delta k_S = k_S - \omega_S/c$, k_S is the wave number of the optical field, ω_S is the circular frequency of the laser, <•••> is the average with respect to all the simulated particles, N is the total number of simulated particles, a and b are the dimensions of the rectangular waveguide, and I is the intensity of the e-beam.

The first term on the right-hand side of equation (1) is the usual energy exchange between electrons and the optical field. The second term is the energy exchange caused by the space charge generated due to electron bunching in the pondero-motive potential well. The phase ψ_i of the electrons in the pondero-motive potential well is expressed by equation (2), where r_i is the spatial position of the electrons which is determined by the Betatron equations, i.e., (3) and (4). The amplitude e_S and phase φ_s of mode TE_{01} are determined by equations (5) and (6). In equation (2), $a_S = e_S/k_S = e|E_S|/1.414 m_0 c^2 k_S$, where $|E_S|$ is the amplitude of the optical field [and 1.414 represents the square root of 2].

In order to verify the reliability and accuracy of the WAGFEL program, a numerical simulation was done based on the actual operation of the ELF facility at LLNL in the United States. The results are basically in good agreement with the experimental data. Hence, the WAGFEL program is reliable. It can be used as a theoretical computing tool for designing the SG-1 FEL.

It is well known that with a constant wiggler the efficiency of an FEL is usually 1/2N, where N is the period of the wiggler. In order to raise the laser output efficiency, it is necessary to use a variable wiggler. This is because with constant parameters the energy of most of the electron bunches captured by the pondero-motive potential well is below the resonance energy when the laser power output reaches saturation. In order to allow these electrons to continue interacting with the optical field to release energy, the resonance energy must also be lowered accordingly to keep the captured electron bunches in an energy-releasing state. From the resonance equation we know that the resonance energy γ_r is:

$$\gamma_r^2 = \frac{\lambda_w}{2\lambda_s} \left[1 + \left(\frac{e\lambda_w B_w}{2\pi m_0 c^2} \right)^2 \right] \qquad (7)$$

In order to lower γ_r it is necessary to change λ_w and B_w. In the actual design of a variable wiggler, it is more difficult to vary λ_w. Therefore, usually B_w is reduced to lower the resonance energy. The key is how to change B_w so that it decreases with the length of the wiggler while ensuring the optimum output efficiency. There are several design methods, including

the single-particle resonance method, declining magnetic-field index method, and multi-particle self-consistency method. Of course, there are more complicated methods which change λ_W and B_W at the same time. However, because of engineering difficulties, they are not being used.

Numerical simulation of SG-1 FEL design parameters shows that the multi-particle self-consistency method is the best. The maximum laser power output is five times the constant parameter saturation power. The single-particle resonance method is the poorest. The maximum power output is only 2.5 times the saturation power with constant parameters. The results are shown in Figure 3. It was decided by comparison that the taper of the wiggler is to be calculated by the multi-particle self-consistency method.

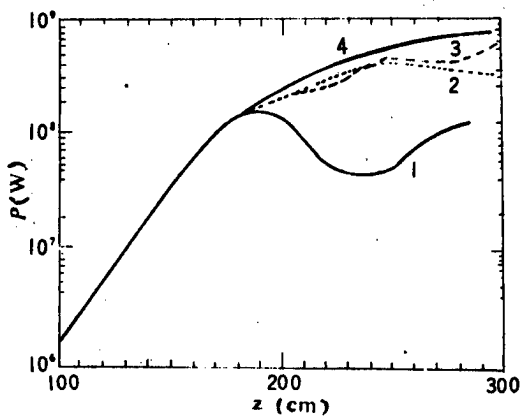

Figure 3. Laser Power P(W) vs. Wiggler Length

Curve 1 is the simulated result of a constant-parameter wiggler. Curve 2 is the simulated result of a variable wiggler designed by the single-electron resonance method. Curve 3 is the simulated result of a variable wiggler designed by the declining-index method. Curve 4 is the simulated result of a variable wiggler designed by the "multi-electron self-consistency method."

Theoretical computations for the SG-1 FEL were carried out using the WAGFEL program. In addition, technical parameters for every component were determined, and are shown in Table 1.

This program was also used to perform a preliminary analysis of the SG-1 FEL device in order to study the effects of certain design parameters on the laser power output and efficiency.

First, let us discuss the effect of e-beam dispersion. It is a very sensitive parameter affecting the gain and efficiency of an FEL. An increase in energy dispersion is equivalent to a larger distribution of electrons in phase space. Consequently, the number of electrons captured by the ponderomotive potential well during the electron/optical-field interaction process is reduced. Hence, when $\Delta\gamma/\gamma$ grows to a certain level, the laser gain is close to zero. Based on numerical simulation, for the SG-1 FEL it is better to have $\Delta\gamma/\gamma$ = 1-3 percent; the maximum should not exceed 5 percent.

Table 1. Technical Parameters of SG-1 FEL

1. linac
energy: $E = 3.5$ MeV pulse beam current: $I = 1.5$ kA pulse width: $\tau = 60$ ns beam radius: $r_e \leq 2$ cm beam brightness: $B_n = 5 \times 10^3$ A/(cm-rad)^2 emittance: $\varepsilon_n = 0.77\ \pi$ cm-rad degree of energy dispersion: $\Delta\gamma/\gamma = 5$ percent
2. beam modulation zone outlet
pulse current: $I = 450$ A effective beam radius: $r_e \leq 0.8$ cm ($a \times b = 0.6 \times 1.2$ cm) beam brightness: $B_n = 4.1 \times 10^3$ A/(cm-rad)^2 emittance: $\varepsilon_n = 0.47$ cm-rad degree of energy dispersion: $\Delta\gamma/\gamma \leq 3$ percent beam waist adjustable range: 2 m
3. wiggler and microwave source
period of magnetic field: $\lambda_w = 11$ cm magnetic field strength: $B_w = 3.1$ kGs taper: $\Delta B_w/B_w > 25$ percent number of cycles of magnetic field: $N = 30$ bidirectional magnetic-field compression ratio: $a = k_y/k_x = 1.4 - 2$ main waveguide dimensions: rectangular 29 x 98 mm waveguide mode: H_{01} microwave source power: $P_{in} = 20$ kW center frequency: $f = 34.6$ GHz
4. FEL output
wavelength: $\lambda_s = 8.67$ mm peak power: $P_{out} > 3 \times 10^8$ W efficiency: $\eta > 20$ percent

Next, let us discuss the effect of emittance. In general, it should be as small as possible because an increase in emittance would lower the small signal gain. However, when the electron beam brightness is fixed, i.e., $2I/\varepsilon_n^2 = \text{const.}$, it is not necessary to lower emittance. This is because when ε_n increases, the beam current goes up proportional to I^2. However, the small-signal gain is proportional to $(I)^{1/3}$ and saturated laser power is proportional to $(I)^{4/3}$. Therefore, both the small-signal gain and saturated laser power can be increased by raising the beam current.

Numerical simulation shows that the effect of the microwave source input power P_{in} is not significant over a large range (100 W-500 kW). Only the position reaching saturated power z_o varies accordingly, i.e., when P_{in} is high z_o decreases and when P_{in} is low z_o increases. Based on the design parameters of the SG-1 FEL, when P_{in} is increased by an order of magnitude, the position to reach power saturation is moved forward by 40 cm. Therefore, the length of the wiggler can be reduced by increasing P_{in}.

III. Physical Design and Research of Different Components of the SG-1 FEL

The physical design and research associated with the 3.5 MeV linac, e-beam modulation system and variable wiggler are described in the following. In addition, the fact that the SG-1 is an experimental facility is taken into account. Hence, the design parameters need to vary over a large range to satisfy various experimental requirements.

(A) The 3.5 MeV Induction Linear Accelerator[3]

The 3.5 MeV induction linac includes the injector, accelerating tube, Marx generator, switch and trigger system, monitoring system and ancillary system. Although the design and manufacture of an induction linac is a relatively mature technology and the physics associated with it is understood, many technical hurdles and engineering problems such as cathode material, cathode structure, synchronization of switching, and increased emittance during beam transport have nonetheless emerged as the quality requirement for the e-beam in an FEL becomes more stringent. These problems in the development of the linac must be resolved, and [equipment] improved and [technology] raised.

1. Injector

The injector is an e-beam source for the accelerator. The performance of the injector affects the quality of the e-beam. In order to meet the SG-1 FEL beam-brightness requirement, it was necessary to investigate ways to increase injector brightness. Initially, the design included two accelerating elements and a diode, to jointly provide 1 MV; there are two more elements for post-acceleration. Figure 4 shows the injector structure. Each accelerating element can generate 250-kV, 100-ns voltage pulses. The diode employs a cold-cathode plane emitter design. After numerous improvements, the final cathode structure is as shown in Figure 5. The cathode material is a velvet emitter, 60 mm in diameter. The diode is surrounded by a focusing coil. The anode is made of stainless steel. There is a 70-mm-diameter hole in the center. The center of this hole is shielded by a 40-mm-diameter tungsten mesh film which is 0.03 mm thick. The electron transmittance is 90 percent. Behind the tungsten mesh is a tapered aluminum collimator with a 40-mm aperture. An axial cathode movement lever can adjust the distance between the cathode and anode. After preliminary tuning, the following specifications were obtained: $E = 1.5$ MeV, $I = 2.7\text{-}3$ kA, $\tau = 90$ ns, beam radius $r_e \leq 2$ cm, $\varepsilon_n = 0.79$ (cm-rad), $B_n = 4.8 \times 10^3$ A/(cm-rad)^2.

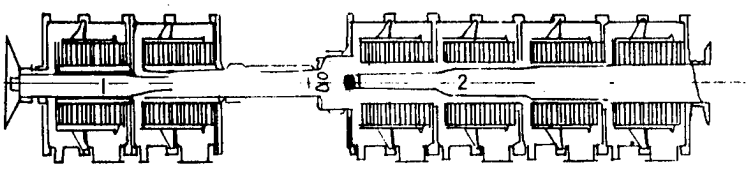

Figure 4. Sketch of the Injector

1 -- cathode rod, 2 -- hollow anode

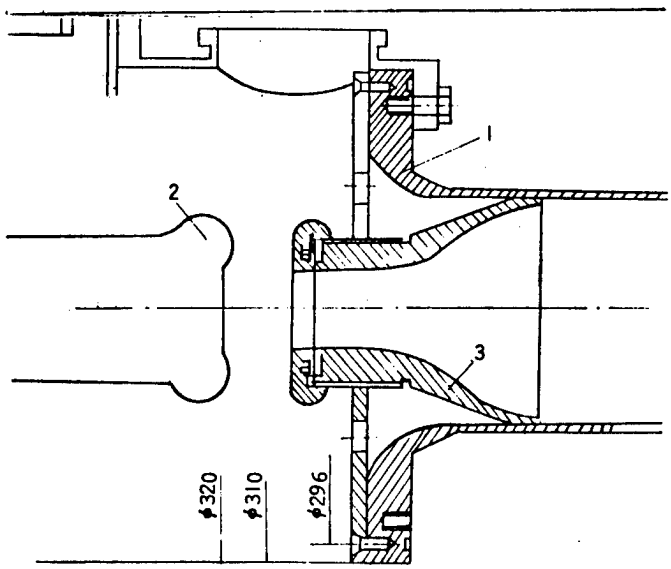

Figure 5. The Diode Structure

1 -- special tube, 2 -- cathode, 3 -- anode

Experimental results obtained at the FXR accelerator in the United States showed that each accelerating element on an average could cause the normalized emittance to go up by 3 percent. The 3.5 MeV LIA [linear induction accelerator] has a total of eight accelerating elements. It is estimated that emittance will increase by a factor of 1.27. Correspondingly, brightness will decrease by a factor of 1.6. Therefore, in order to meet the design specification, the injector brightness must be raised to 10^4 A/(cm-rad)^2. Based on the experimental conditions, the brightness calculated by the SLAC-226 simulation program is 2×10^4 A/(cm-rad)^2. The theoretical value is four times higher than the experimental data. Hence, it is possible to raise the injector brightness further under existing conditions.

Ways To Raise Injector Brightness

(1) Increase the diode field strength. As the diode field increases, the emission current goes up and the beam current also rises. In addition, an increase in field strength also leads to an increase in the longitudinal momentum of electrons. Thus, emittance decreases and beam brightness increases. The experimental result shown in Figure 6 was obtained by Professor G. Bekefi at MIT.[4] Of course, increasing field strength is limited by electrical breakdown. Furthermore, it is necessary to prevent emission of electrons from non-emitting surfaces and avoid strong space-charge effects.

(2) Decrease collimation ratio. The collimation ratio is defined as the ratio of the current entering the anode hole to the current emitted by the cathode. Usually, the field is stronger at the center of the cathode and the brightness is higher. To decrease the collimation ratio is to introduce the brighter electron beam near the center into the accelerating section. It was experimentally verified that maximum beam brightness is obtained when the

collimation ratio is around 0.2.[5] The collimation ratio of the 1 MeV injector is approximately 0.3-0.25; therefore, it can be adjusted to raise the brightness more.

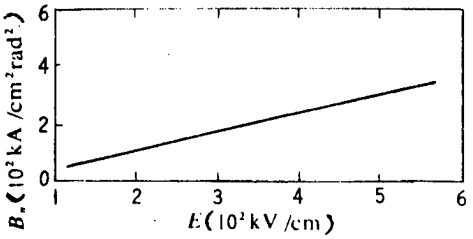

Figure 6. Experimental Curve of Diode Field of Velvet Cathode vs. Beam Brightness

(3) Change cathode and anode materials and structure. Beam brightness can be optimized by varying the anode-cathode structure and the magnetic field distribution in the diode, i.e., adjusting the electro-optical system.[6] Different cathode materials would yield different beam brightnesses. For a one-time-operated LIA, the majority of experimental data demonstrates that a cathode fabricated from velvet material produces the best results.

(4) Use a pentode to raise brightness. This is an unusually effective technique for increasing beam brightness. According to an LLNL report, with a velvet cathode, the beam brightness is as high as 4×10^4 A/(cm-rad)^2 with the optimum diode design. However, when using a pentode electron gun,[7] it is as high as 2×10^5 A/(cm-rad)^2. We have done some preliminary calculations on using a pentode electron gun and estimated that it is possible to raise the beam brightness by an order of magnitude. Figure 7 shows the simulated electron-gun trajectory. At 32 cm from the cathode, the brightness is 10^5 A/(cm-rad)^2.

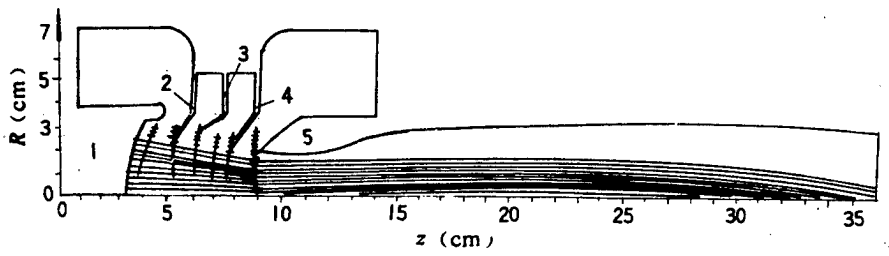

Figure 7. Electron Trajectory in a Pentode

1 -- cathode, 2 -- first anode, 3 -- second anode, 4 -- third anode, 5 -- fourth anode

2. Accelerating Element

The 3.5 MeV LIA has a total of 12 accelerating elements. Four of them form the injector and the remaining eight form the acceleration section. Figure 8 shows the cross section of an accelerating element. Figure 9 is a schematic diagram of an accelerating element. It includes a cavity, ferrite core, beam path, focusing solenoid coil, MC nylon insulator, Blumlein feeder and stabilizing resistor. Table 2 lists the technical specifications of the ferrite ring.

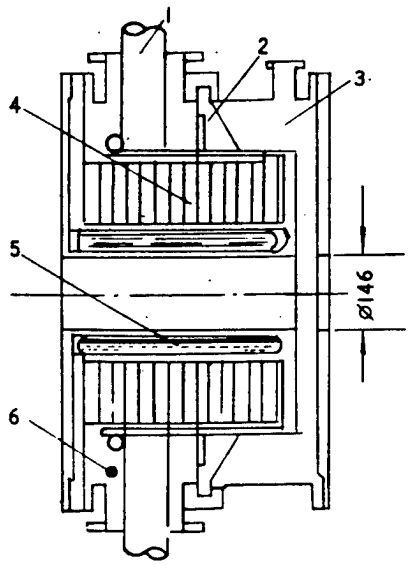

Figure 8. Cross Section of the Accelerating Element

1 -- feeder and stabilizing resistor, 2 -- epoxy insulating ring, 3 -- vacuum, 4 -- ferrite ring, 5 -- focusing coil, 6 -- oil

The diameter of the e-beam transport channel is 146 mm. The gap between accelerating elements is 45 mm. An MC-6 nylon ring is used to separate the oil from vacuum. Near the transport channel, there is a non-uniform solenoid to generate a 0.1-0.2 T axial magnetic field to minimize e-beam diffusion. In the accelerating section, four accelerating elements are put in series to form a section. Each element has a Blumlein feeder. The four Blumlein feeders are powered by a Marx generator. There is a transition segment between sections and a bridging coil is installed to maintain the continuity of the axial magnetic field. In addition, there is a pair of regulating coils every two or three sections to provide proper adjustment in the x, y direction in case of deviation.

3. Pulse Generator and Marx Generator

The Marx generator is the primary power source for the pulse generator (Blumlein line). Each Marx generator charges four Blumlein lines. A total of three Marx generators are needed. A Marx generator uses low-inductance pulse capacitors (MY100-0.63) to store energy. Its design parameters are shown in Table 3.

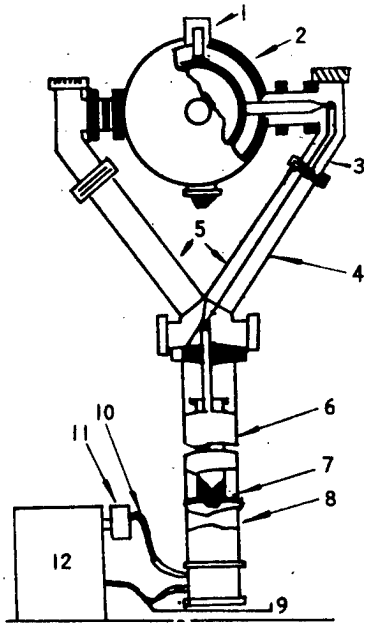

Figure 9. Schematic Diagram of the Accelerating Element

1 -- stabilizer load, 2 -- cavity, 3 -- oil, 4 -- water, 5 -- feeder, 6 -- Blumlein line (10Ω), 7 -- insulating plate, 8 -- spark-gap switch, 9 -- charging cable, 10 -- trigger cable, 11 -- switch II, 12 -- Marx generator

Table 2. Technical Specifications of the Ferrite Ring

Dimensions (mm)	outer diameter	508
	inner diameter	254
	thickness	25
800 A/m excitation		$B_s \geq 0.38$ T
		$B_r \geq 0.26$ T
Minimum resistivity ρ (Ω-cm)		$\geq 3 \times 10^6$
Maximum coercive force H_e (A/m)		< 55
Dielectric strength		Voltage resistance ≥ 120 kV when applying 90-ns pulses on 25-mm-thick ferrite in oil

Table 3. Design Parameters for the Marx Generator

Item	Parameter
Stages	10
Capacitance per stage	1.26 μF
Impulse capacitance	126 nF
Maximum charging voltage	± 50 kV
Internal inductance	< 2 μH
Pulse output jitter time	< 30 ns
Series inductance	approx. 46 μH
Maximum nominal energy storage	15.75 kJ

At the output of the Marx generator, there is a 46-μH inductor in series to adjust the amplitude of the charging current for the Blumlein lines in order to meet the reset current and reset time requirements.

The pulse generator is a coaxial Blumlein line using water as the dielectric medium. Its special features include low impedance, high energy-storage density, ability to recovery from breakdown, non-production of any conductive matter and absence of pollution. All Blumlein lines and feeders were designed to operate at 400 kV to ensure reliable tolerance to high voltage. At 250 kV, each Blumlein can release 500 J of energy. After taking rise time and jitter time into account, in order to ensure the e-beam output has a 60-ns plateau, the half-height width (FWHM) of the Blumlein is designed to be 90 ns. Its design parameters are shown in Table 4.

Table 4. Blumlein-Line Design Parameters

Inner conductor	i.d. --- o.d. 67 mm	
Middle conductor	i.d. 149 mm o.d. 152 mm	
Outer conductor	i.d. 346 mm o.d. 356 mm	
Inner transmission line	intrinsic impedance	$Z_1 = 5.4\ \Omega$
	electric field at 400 kV	$E_1 = 149$ kV/cm
	rated breakdown field (1 μs)	$E_{BD1} = 300$ kV/cm
Outer transmission line	intrinsic impedance	$Z_2 = 5.4\ \Omega$
	electric field at 400 kV	$E_2 = 64$ kV/cm
	rated breakdown field (1 μs)	$E_{BD2} = 152$ kV/cm
Dielectric: water	resistivity $\rho \geq 3$ MΩ-cm	
Polarity of middle conductor: positive		

4. Switch and Trigger System

The operating process of the LIA is first to use Marx generators to charge up the pulse generating lines and then trigger the main switch to discharge the pulse generator in order to generate synchronized accelerating voltage pulses at the gap. In order to achieve synchronized acceleration of the e-beam from various gaps, there is a stringent requirement for the jitter time of the entire system. This is a key technology for obtaining a synchronized and stable linear accelerator.

Based on design requirements, we can calculate that the maximum jitter between the beam current and accelerating pulse is ± 15 ns, with an rms value of 5 ns. The trigger has a three-stage structure. Let us assume that all switches have identical operating states and the jitter time is σ_i. Because the three stages are in series, if other jittering factors (such as jitter of the injected beam) are not considered, then the jitter time of each switch should be less than $5/(3)^{1/2}$ = 2.88 ns.

Figure 10 shows the block diagram of the trigger system. The overall relative jitter of the closed system and its effect on the amplitude of the accelerator voltage can be estimated.

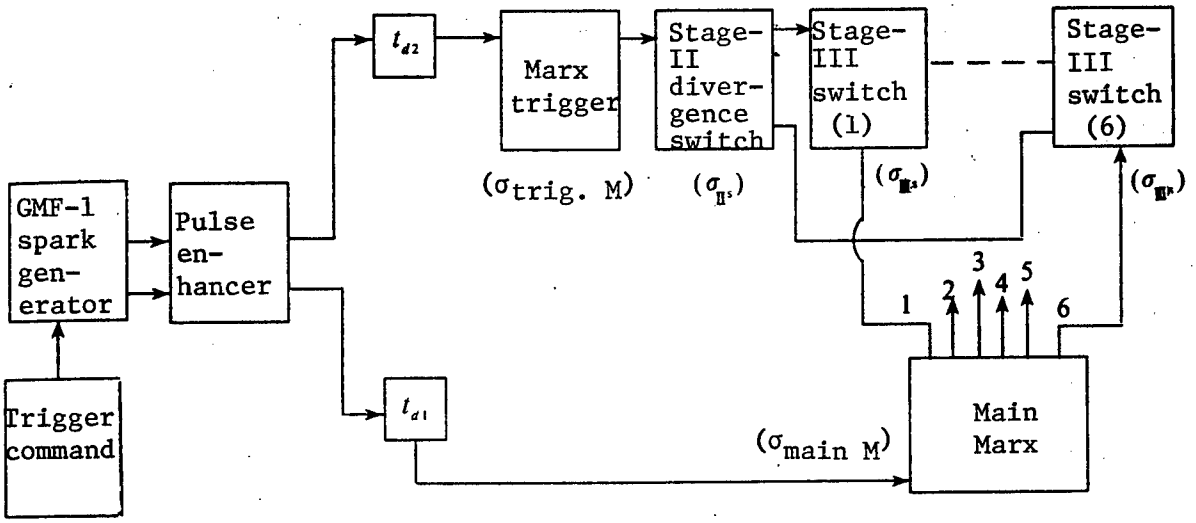

Figure 10. Block Diagram of the Injector Circuit

[The equation for overall jitter is:]

$$\sigma_T = \sqrt{\sigma^2_{trig.M} + \sigma^2_{II\,S} + \sigma^2_{III\,S} + \sigma^2_{main\,M}} \qquad (8)$$

where the stage difference $\Delta T_m = 3\ \sigma_T$. Hence, the charging voltage amplitude on the Blumlein line varies according to:

$$\eta = \frac{V_{Bm} - V_{Bj}}{V_{Bm}} = \frac{1}{2}\left[1 + \cos\pi\left(1 - \frac{3\sigma_T}{T_m}\right)\right] \qquad (9)$$

where V_{BM} is the maximum Blumlein discharge voltage, V_{Bj} is the actual Blumlein discharge voltage, and T_m is the maximum charging time to reach highest charging voltage.

The effect of jitter time of the closed system on the amplitude of the accelerating voltage is shown in Figure 11. Based on the energy dispersion requirement, it can be calculated that the jitter of the closed system must be $\leq$ 50 ns.

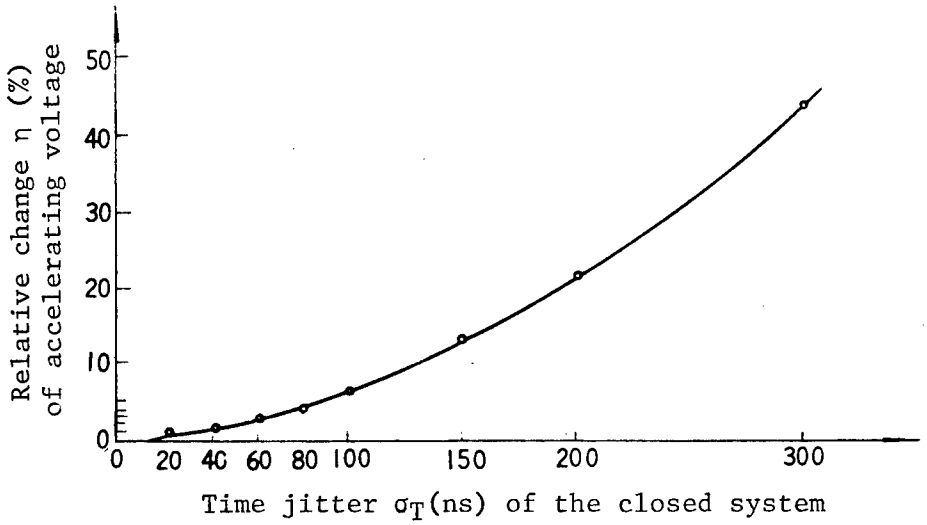

Figure 11. Effect of Jitter Time of the 1.5 MeV LIA Closed System on the Amplitude of the Accelerating Voltage

(B) E-Beam Transport System

The e-beam transport system consists of two parts: the beam transport system inside the accelerator and that in the modulation zone. The mission of the beam transport system is to overcome space-charge effects and beam instability during the process of e-beam drift and acceleration in order to ensure stable transport. Thus, the beam current loss and any increase in normalized emittance are minimized to the extent possible and design requirements such as energy dispersion and beam radius can be met.

1. Beam Transport System in the Accelerator

The usual beam transport methods for an LIA include a solenoid-focusing magnetic field, quadrupole magnetic field and ionic channel (laser-guided), etc. Nevertheless, lower-energy accelerators usually use the solenoid-focusing magnetic field. Therefore, this system also uses a solenoid-focusing magnetic-field scheme. The injector has seven solenoids and the accelerating section has 16 solenoids. There is a bridging coil and a

beam-control coil between the accelerating section and the injector. There are two bridging coils and one control coil between elements. Between the output of the accelerating section and the modulation zone, there are two bridging coils and a control coil. The function of the bridging coil is to maintain the continuity of the focusing magnetic field. The control coil, however, generates a transverse magnetic field to correct the beam position. Each coil is powered by an independent power supply and the current level is continuously tunable. All coils and power supplies are water-cooled.

Due to various factors an e-beam will suffer emittance increase and beam current loss during the transport and acceleration process. The following issues must be addressed in designing a transport system:

(1) Effect of magnetic field fluctuation at acceleration gap

Because the continuity of the magnetic field is interrupted by the acceleration gap, the field fluctuates and causes transverse disturbance of the beam. This leads to an increase in emittance, especially more significant at lower energy. Therefore, fluctuation must be held to a minimum in the low-energy region. The main measure to reduce fluctuation is to shorten the distance between the ends of neighboring coils. Next, non-uniformly wound coils are used.

(2) Effect of lateral drift of beam center

Lateral drift of beam center would lead to a loss of beam current, and eventually to its collapse. There are two factors contributing to the lateral drift: One is the effect of helical motion. Since there is a finite energy dispersion in the e-beam pulse, these electrons have different Betatron wavelengths in the solenoid-focusing magnetic field. Thus, the transverse displacement of the beam center varies with time. The amplitude of change is eventually comparable to that of the initial displacement. Its frequency increases as a function of the axial propagating distance which excites the acceleration cavity to go into resonance and leads to beam collapse. To suppress lateral drift due to helical motion, energy dispersion and axial magnetic field must be reduced. Another factor is BBU instability. Because continuity of the beam channel is interrupted by the acceleration gaps, when an e-beam with a slight lateral drift enters a gap, the cavity is excited to generate the transverse magnetic dipole mode TM_{1n}. The transverse component of the magnetic field will apply a lateral impulse to the e-beam to cause further displacement of the beam center. As the gap increases, this lateral displacement would go up rapidly which eventually leads to beam collapse. Therefore, for a very long or strong beam current linac, the magnitude of the transport current is limited by BBU instability. An effective way to suppress BBU instability is to enhance the focusing magnetic field. However, this would increase the effect of helical motion on the lateral drift of the beam center. Hence, the strength of the magnetic field must be determined after taking both factors into consideration.

(3) Effect of non-linear space charge

Effect of non-linear space charge also causes increased emittance. In part, excess space-charge potential is converted into lateral thermal motion. Furthermore, the space-charge potential is a radial function of the beam and is dependent on the beam radius. Therefore, if the radius can be held to a minimum during the transport process, then any increase in emittance can also be kept at a minimum.

(4) Beam alignment

Beam alignment is a key issue to ensure stable transport. It primarily involves the geometric alignment of the channel and the alignment of the focusing magnetic field. The design specification is ± 1 mm.

Two factors must be considered in the alignment of the magnetic axis. One factor involves the effects of axial symmetry of the magnetic field of the coil, direction of the lead wires, and other environmental aspects such as the presence of paramagnetic matter and the Earth's magnetic field. The other factor is the precision installation of the focusing solenoids, bridging coils and control coils along the beam channel. In particular, special installation procedures must be used for short coils.

2. Beam Transport in the Modulation Zone[8]

The primary functions of the beam transport system in the modulation zone are to maintain the quality of the beam, minimize energy dispersion, and match the accelerator with the wiggler. The position of the e-beam waist in the wiggler can be controlled by varying the field strength of the quadrupole magnetic lens. The modulation zone includes devices such as a magnetic collimator, energy-selective grating, quadrupole lens, and beam-position controller.

Since the beam-current quality factor Q is proportional to its density J and is inversely proportional to the degree of effective axial energy dispersion $\Delta\gamma_z/\gamma$, i.e.,

$$Q = \frac{J}{(\Delta\gamma_z/\gamma)} \tag{10}$$

in order to improve quality, on one hand we must raise current density and on the other hand we must reduce $\Delta\gamma_z/\gamma$. The effective axial energy dispersion consists of the following components:

Dispersion of kinetic energy of electrons

$$\left(\frac{\Delta\gamma_z}{\gamma}\right)_{\Delta E} = \frac{\Delta E}{E} \tag{11}$$

Effective energy dispersion due to emittance

$$\left(\frac{\Delta\gamma_z}{\gamma}\right)_{\varepsilon_n}=\frac{1}{2}\left(\frac{\varepsilon_n}{r}\right)^2 \tag{12}$$

Effective energy dispersion caused by space-charge effect

$$\left(\frac{\Delta\gamma_z}{\gamma}\right)_{sc}=\frac{1}{\gamma}\left(\frac{\omega_v r}{2c}\right)^2 \tag{13}$$

Effective energy dispersion due to magnetic field gradient of the wiggler

$$\left(\frac{\Delta\gamma_z}{\gamma}\right)_{w}=\left(\frac{\Omega_w r}{2c}\right)^2 \tag{14}$$

Usually, the contribution from the two latter terms is small and can be neglected. Hence, ε_n and $\Delta E/E$ are the two major factors affecting beam current quality. One of the objectives of beam current modulation is to limit its emittance and the range of $\Delta E/E$.

(1) Magnetic collimator

The function of this device is to select the beam current emittance. The device, whose structure is shown in Figure 12, is connected to the exit of the accelerator through a high-vacuum valve.

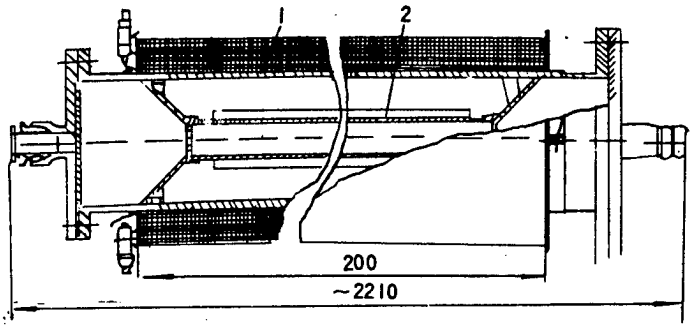

Figure 12. Structure of the Magnetic Collimator

1 -- magnetic field coil, 2 -- collimator tube

The major technical parameters of the collimator are as follows:

Collimating hole diameter	2R = 2.6 cm
Collimating hole length	L = 1.924 m
Magnetic field strength	B_0 = 0.01 - 0.1T tunable
Adjustable range for	ε_n = 0.1 - 1 (π-rad-cm)

A double-wire winding coil is used. It can be connected to a dc power supply either in parallel or in series to increase the tunable range. The dc power supply is a constant-current source with a stability of 5×10^{-4}.

(2) Quadrupole lenses

The function of these devices is to focus the e-beam and to adjust the beam cross section. Structurally, it is required to be able to adjust position in all directions. The combined effect of the second and third pair of quadrupole lenses makes waist-to-waist transport and transformation possible to meet the requirements for the wiggler in its interaction zone. The parameters for the quadrupole lens are: effective aperture 2a = 14 cm, magnetic field gradient G = 0.5-6 T/m tunable, magnetic pole length L = 25 cm.

The center of the magnetic pole is hyperbolic and its equation is:

$$x \cdot y = 2450 \ (\text{mm}^2) \qquad (15)$$

[A view of the quadrupole lens is given in Figure 13.]

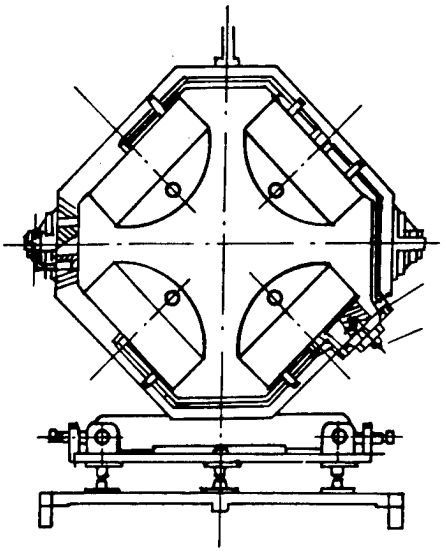

Figure 13. Longitudinal View of the Quadrupole Lens

(3) Optical grating and control coil

The optical grating and the first pair of quadrupole lenses form an energy-selection system. The energy distribution of the accelerated e-beam can be reduced by this device. The shape and size of the grating aperture is changeable. The position of the grating plate can also be adjusted by a moving mechanism within a range of ± 12 cm. It can also be connected to the energy measuring device for automatic feedback control.

The control coil behaves similarly to the control coils in the accelerator. It is a critical component which ensures the alignment of the e-beam. In the modulation zone, there are three control coils. Each coil is elliptical in shape and can work in conjunction with the beam position detector. The current in the coil is controlled based on the actual measured deviation from the center. The designed deviation is y = 0.5 cm/m.

(C) Wiggler

The wiggler is where the energy exchange between the e-beam and the laser field takes place. The design of the wiggler will directly affect the efficiency of energy extraction from the e-beam. After an analysis, we chose to use a linearly polarized pulse electromagnetic wiggler. The surface of the magnetic pole is parabolic in shape in order to focus the e-beam in a bidirectional manner. The reason for using a pulsed electromagnet is to reduce the energy requirement of the power source. Moreover, it is easier to adjust the magnetic field, does not require a cooling system, and costs less. In addition, the magnetic field can be adjusted over a wide range to facilitate different taper requirements. However, problems such as stability, synchronization and homogeneity of the magnetic field strength must be addressed when a pulsed electromagnet is used. Because the e-beam is relatively short, only tens of nanoseconds, as long as the magnetic field is sufficiently wide (e.g., milliseconds) and the trigger system is well synchronized, and the power supply is stable, then the stability, synchronization and homogeneity requirements of the magnetic field are easily attainable. As for an FEL with a high repetition frequency, either a dc electromagnet or a permanent-magnet wiggler must be used.

In the design of the high-efficiency wiggler, the following key technical issues must be addressed:

(1) Focusing the e-beam in the wiggler

In the wiggler, electrons in the beam will expand due to the force of space charge which causes its emittance to rise. Consequently, the number of electrons captured by the pendero-motive potential well is reduced and the gain is lowered. Furthermore, it also affects the excellent match between the e-beam and laser envelope. Sometimes, it exceeds the "envelope constraint" condition. For an FEL, the envelope constraint is $\varepsilon_n \leq \gamma\lambda_s/2$. When the wavelength of radiation λ_s is very short, the e-beam emittance requirement is very stringent. It must be capable of bidirectional focusing of the e-beam. In a circularly polarized wiggler, the magnetic field of the wiggler has bidirectional focusing capability with respect to the e-beam. In a linearly polarized wiggler, it can only focus in the direction of the magnetic field (i.e., y direction). It cannot focus in the x direction. Hence, it is necessary to add another focusing force. The common focusing magnetic field includes a helical coil field, a quadrupole field and a hexapole field. A hexapole field can be replaced by an equivalent parabolic magnetic pole. E. T. Scharleman pointed out that a parabolic magnetic pole is the preferred way to realize bidirectional focusing of an e-beam[9] because a hexapole field can prevent Betatron instability. Thus, the focusing effect is more uniform

without any ancillary coils and excitation power supply. The effectiveness of the parabolic magnetic pole has been verified experimentally by Paladin in the United States. The disadvantage of this magnetic pole is that the gap height is increased. Consequently, the field strength is lowered. There are three ways to overcome this problem. One is to use an elliptical or circular waveguide to replace the rectangular waveguide to reduce the gap. Since an elliptical waveguide has the singular H_{11} mode which is similar to the H_{01} mode in a rectangular waveguide, it is in principle feasible. Second is to use a hybrid pole with permanent-magnet compensation, such as the Paladin wiggler built by M. J. Burns and associates at LLNL using an electromagnet as the basic structure together with $SmCO_5$. In order to raise the magnetic field further, they also proposed schemes such as the "strong electromagnet" and "inlaid electromagnet." These hybrid magnets have one thing in common, i.e., using $SmCO_5$ to reduce magnetic leakage flux at the edges of the basic electromagnet. But, they are more expensive to make. A third way is the "magnetic shield" pulsed electromagnet,[10] i.e., adding an additional non-magnetic metal plate between two neighboring magnetic poles. When a pulse magnetic field is present, the metal plate generates an eddy current and an induced magnetic field. This magnetic field can significantly weaken the leakage flux between neighboring poles. Hence, the magnetic field strength of the wiggler can be raised. Experimentally, it was found that inserting a 6-mm-thick aluminum plate between neighboring poles can raise the magnetic field by more than 15 percent. As shown in Figure 14, this is easy to build and costs less.

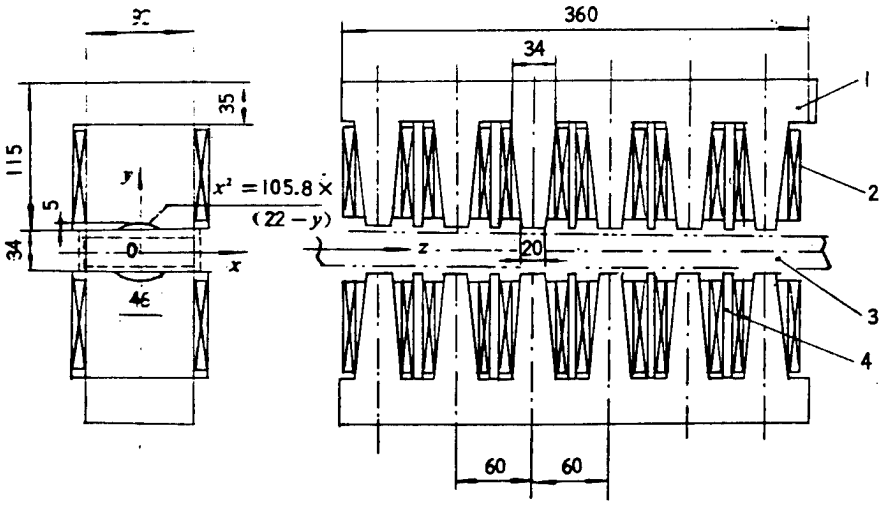

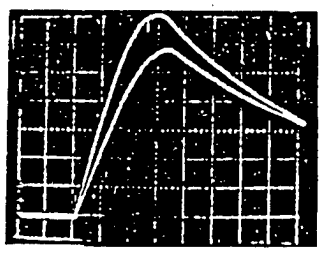

Ordinate: 630Gs/div.
Abscissa: 100μs/div.
Upper: with Al plate
Lower: without shield

Figure 14. Scheme and Experimental Results of the Shielded Pulsed Electromagnet

1 -- magnetic pole, 2 -- excitation coil, 3 -- microwave waveguide, 4 -- shield

The focusing power of the parabolic magnetic pole is analyzed as follows. In a parabolic wiggler, the transverse magnetic-field distribution can be written as:

$$B_w = B_{w0} \cos h\, k_x x \cos h\, k_y y \cos k_w z \tag{16}$$

$$k_x^2 + k_y^2 = k_w^2 \tag{17}$$

The variations of the magnetic field in the x and y direction can be written separately as:

$$\Delta B_{wx} / B_{w0} = \frac{1}{2} k_x x_0^2 \tag{18}$$

$$\Delta B_{wy} / B_{w0} = \frac{1}{2} k_y y_0^2 \tag{19}$$

where x_0 and y_0 are the cross-section dimensions of the e-beam at the entrance of the wiggler. Define focusing power as $\alpha = k_y/k_x$, which is the square root of the ratio of the y-direction focusing power of the wiggler to the x-direction focusing power. Numerical calculations were made with different values of α and the results showed that $\alpha = 2$ is the best choice. Of course, it is also dependent upon the transverse distribution of the e-beam. When λ_w = 11 cm and B_w = 3100 Gs, the output power verses α varies as shown in Figure 15. From the figure, we can see that there is very little difference when α = 1-2.

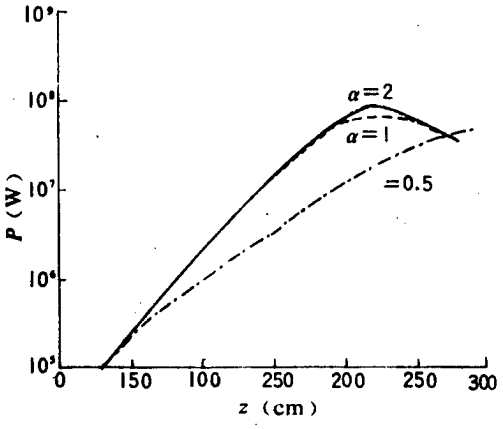

Figure 15. Effect of Focusing Power of Parabolic Magnetic Pole (α) on the Output Power (λ_w = 11 cm, B_w = 3100 Gs)

(2) Design of transition zone at the inlet of the wiggler

Whether the e-beam can enter the wiggler smoothly and maintain its high quality is critically dependent upon the design of the transition zone at the inlet of the wiggler. In general, a good adiabatic inlet design must meet three conditions, i.e., resonance condition, minimum Betatron resonance amplitude condition and e-beam shape-matching condition. Specifically,

(a) no discontinuity of the magnetic field in the inlet, (b) the inlet zone must meet a certain length requirement in order to allow the e-beam to enter the wiggler zone without significant deterioration of energy dispersion and emittance, and (c) the inlet should not be too long to make it difficult to focus. The second and third points conflict with each other. On one hand, the inlet should be as long as possible to minimize kinetic energy dispersion during injection. On the other hand, as the inlet gets longer, the length where B_W increases also becomes longer. Thus, the focusing power is less and the beam current would collapse very rapidly. This is even more obvious at higher current. Therefore, a comprehensive consideration is necessary.

There are two approaches to the inlet problem. (a) A longer inlet transition zone is used for circularly polarized wigglers. In addition, an additional axial magnetic field is used for focusing. Usually, the inlet wiggler period is $N > 5$. (b) A short inlet transition zone is used for linearly polarized wigglers.

As for the inlet transition zone for the SG-1 FEL, an analysis shows that it is more appropriate to use a short transition zone. Preliminarily, the magnetic field amplitude was chosen to vary according to the following function:[12]

$$B_w(z) = B_{w0} \sin\left(\frac{k_w z}{4N}\right) \qquad (20)$$

IV. Conclusions

The above is an introduction to the design and development of the SG-1 FEL. In the area of theoretical simulation, the WAGFEL program was employed. The ELF experimental data obtained by LLNL were used to verify our results and they were found to be in excellent agreement. Major technical specifications for the hardware were determined based on theoretical design. The physical design of various hardware components was completed in conjunction with experiments on prototypes. This paper points out certain key issues encountered in the design and development of the linac, beam modulation system and wiggler.

Based on the multi-particle self-consistent method, the power output of the SG-1 FEL is estimated to reach 3×10^8 W with efficiency greater than 20 percent. If the accelerator can provide higher current and better current quality, then the output power of the SG-1 FEL can reach 10^9 W and efficiency over 30 percent.

Acknowledgement

Tao Zucong [7118 4371 5115], Zhao Weijin [6392 4850 2516], Zhang Shouyun [1728 1108 0061], Ding Bonan [0002 0130 0589], Cheng Nianan [4453 1819 1344], Yang Zhenhua [2799 7201 5478], Zhou Chuanming [0719 0278 2494], Su Yi [5685 3015], Hu Kesong [5170 0344 2646], Huang Sunren [7806 1327 0088], and Wang Mingli [3769 2494 4409] have contributed to this work. The results of their investigation and design work have been reviewed and used.

References

1. Yang Zhenhua, Tian Shihong [3944 0013 3163], Dong Zhiwei [5516 1807 0251], and Wang Chuntai [3769 2594 3141], "Theoretical Computation of 3.5 MeV Millimeter-Wave FEL," Symposium of the Fourth Annual FEL Meeting of China Institute of Engineering Physics, 5-18 (1989).

2. T. J. Orzechowski, E. T. Scharleman, S. M. Yarema, D. B. Hopkins, A. C. Paul, A. M. Sessler, and J. S. Wurtele, IEEE J. QUANTUM ELECTRON., QE-21, 831 (1985).

3. Zhang Shouyu, "Physical Engineering Design Scheme for 4 MeV LIA," Symposium of the Fourth Annual FEL Meeting of China Institute of Engineering Physics, 19-30 (1989).

4. G. Bekefi, R. E. Shefer, and S. C. Tasker, "Beam Brightness From a Relativistic Field-Emission Diode With a Velvet-Covered Cathode," NUCLEAR INSTRUMENTS AND METHODS IN PHYSICS RESEARCH, A 250, 91-94 (1986).

5. B. Kulke and R. Kihara, "Emittance Measurements on Field Emitter Diodes," UCRL-825, 5 April 1979.

6. L. Schlitt and G. Proulx, "High-Brightness Cathode Experiments on the Experimental Test Accelerator (ETA)," UCRL-15660.

7. G. J. Caporaso and D. L. Birx, "Brightness Measurements on the Livermore High-Brightness Test Stand," IEEE TRANSACTIONS ON NUCLEAR SCIENCE, NS-32 (5), 1985.

8. Huang Sunren, "Engineering Design of Electron Beam Modulation System in SG-1," Symposium of the Fourth Annual FEL Meeting of China Institute of Engineering Physics, 50-56 (1989).

9. E. T. Scharleman, "Wiggler Plane Focusing in Linear Wigglers," J. APPL. PHYS., 58 (6), 1985.

10. Zhou Chuanming and Wang Mingli, "Pulse Electromagnetic Wiggler With Magnetic Shielding, QIANG JIGUANG YU LIZI SHU [HIGH-POWER LASER AND PARTICLE BEAMS], 1 (2), 1989.

11. D. C. Cquimby, et al., IEEE TRANS., QE-21, 988-999, 1985.

12. Zhou Chuanming and Meng Fanbao [1322 0416 1405], "Preliminary Investigation of Wiggler Inlet Design," Symposium of the Fourth Annual FEL Meeting of China Institute of Engineering Physics, 1989.

Radiation Transmission of Free Electron Laser in Terms of Waveguide Laser Theory

91FE0498A Shanghai ZHONGGUO JIGUANG [CHINESE JOURNAL OF LASERS] in Chinese Vol 18 No 2, Feb 91 pp 81-84 [MS received 3 Jul 90]

[Article by Wang Mingchang [3769 2494 7022] of Shanghai Institute of Optics and Fine Mechanics, CAS: "Radiation Transmission of Free Electron Laser in Terms of Waveguide Laser Theory"]

[Text] Abstract

In this paper a new method is proposed to treat the transmission of free electron laser (FEL) with waveguide laser theory. The study shows that there is a low-loss transmission mode. The electromagnetic field is in the EH_{11} mode in the dielectric waveguide. The mode-coupling loss is also discussed.

In an FEL, the magnetic field gap in the wiggler should be as small as possible in order to have a higher field in the center. The length of the wiggler should be long so that the gain from mutual interaction is high. Under such conditions, the slender waveguide in the wiggler places some constraints on the radiation field, just as a waveguide laser cavity.

Existing FEL theory considers the interaction between the wiggler field and the electron beam. This is useful in determining the gain and efficiency of the device. However, the transmission mode is not taken into account. This special situation involving a slender waveguide and wavelength far less than the waveguide has not been considered in microwave theory and laser theory as well.

In this paper, an attempt is made to treat the transmission of FEL radiation mode using the waveguide laser theory to calculate its transmission loss. The results indicate that there is a specific low-loss transmission mode. In addition, a dielectric waveguide can be used instead of a metal waveguide. In a dielectric waveguide, the low-loss mode is EH_{11} and its transmission loss factor is 8.5×10^{-3} dB/M. A metal waveguide has a higher transmission loss. The mode-coupling loss in the cavity depends on the structure of the cavity.

I. Theoretical Model

For simplicity, let us consider the cylindrical waveguide shown in Figure 1. Its radius is a and the free-space dielectric constant is ε_0. The waveguide wall is either made of a dielectric or metal and its dielectric constant is ε. Its magnetic permeability is μ_0 which is identical to that in vacuum.

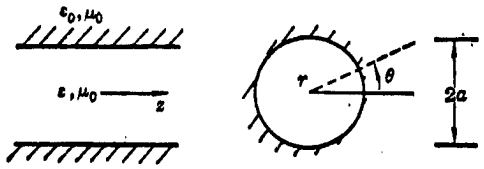

Figure 1. Schematic Diagram of the Cylindrical Dielectric Waveguide

The transmission characteristics of metallic waveguide are well known at microwave frequency. However, the theory is not applicable to optical frequency because metal neither behaves like a good conductor nor a dielectric with a high dielectric constant. As a matter of fact, both metal and dielectric waveguides can be considered as hollow cylinders.

Assume the following conditions are satisfied in the waveguide:

$$Ka \gg |\nu| u_{nm} \tag{1}$$

$$|\gamma/K - 1| \ll 1 \tag{2}$$

We are only considering the situation wherein the radius of the waveguide is much larger than the vacuum wavelength λ; radiation is bouncing off the wall at the grazing angle. Most of the energy is transmitted inside the waveguide and only a small portion is lost due to refraction. u_{nm} is the mth root of the Bessel function $J_{n-1}(u_{nm}) = 0$ and $\nu = (\varepsilon/\varepsilon_0)^{1/2}$ is the complex index of refraction of the waveguide wall. Equation (2) assumes that the mode transmission constant γ is close to the transmission wave number K, which limits the analysis for low-loss modes.

The electromagnetic component of a complex mode in the waveguide is:[1]

$$\left.\begin{aligned} E^{\theta}_{nm} &= \left[J_{n-1}(K_t r) + \frac{i u_{nm}^2}{2nKa}\sqrt{\nu^2-1}\, J'_n(K_t r)\right]\cos n\theta \\ E^{r}_{nm} &= \left[J_{n-1}(K_t r) + \frac{i u_{nm}^2}{2Kr}\sqrt{\nu^2-1}\, J_n(K_t r)\right]\sin n\theta \\ E^{z}_{nm} &= -i\frac{u_{nm}}{Ka} J_n(K_t r)\sin n\theta \end{aligned}\right\} \times \exp[i(\gamma z - \omega t)] \tag{3}$$

$$H^{\theta}_{nm} = \sqrt{\varepsilon_0/\mu_0}\, E^{r}_{nm}$$

$$H^{r}_{nm} = -\sqrt{\varepsilon_0/\mu_0}\, E^{\theta}_{nm}$$

$$H^{z}_{nm} = -\sqrt{\varepsilon_0/\mu_0}\, E^{z}_{nm} \operatorname{ctg} n\theta$$

where the relation between the complex transmission constant γ and the intra-waveguide wave number K_i is:

$$K_i^2 = K^2 - \gamma^2 \tag{4}$$

Here, n and m are the number of cycles of the radiation field in the θ and radial directions, respectively.

In a hollow cylindrical dielectric waveguide, the lowest-loss mode and the most interesting mode is EH_{11}. In a cylindrical coordinate system, its six field components are:

$$\begin{aligned}
E_{11}^{\theta} &= J_0\left(u_{11}\frac{r}{a}\right)\cos\theta\exp[i(rz-\omega t)] \\
E_{11}^{r} &= J_0\left(u_{11}\frac{r}{a}\right)\sin\theta\exp[i(rz-\omega t)] \\
E_{11}^{z} &= -i\frac{u_{11}}{Ka}J_1\left(u_{11}\frac{r}{a}\right)\sin\theta\exp[i(rz-\omega t)] \\
H_{11}^{\theta} &= \sqrt{\varepsilon_0/\mu_0}E_{11}^{r} \\
H_{11}^{r} &= -\sqrt{\varepsilon_0/\mu_0}E_{11}^{\theta} \\
H_{11}^{z} &= -\sqrt{\varepsilon_0/\mu_0}E_{11}^{z}\operatorname{ctg}\theta
\end{aligned} \tag{5A}$$

where θ and r are the angular and radial components of the cylindrical coordinate system, respectively.

In a hollow cylindrical metal waveguide, the field distribution of the lowest-order transverse electrical mode TE_{01} is:

$$\begin{aligned}
E_{01}^{\theta} &= J_1\left(u_{01}\frac{r}{a}\right)\exp[i(\gamma z-\omega t)] \\
H_{01}^{r} &= -\sqrt{\varepsilon_0/\mu_0}E_{01}^{\theta} \\
H_{01}^{z} &= -i\sqrt{\varepsilon_0/\mu_0}\left(\frac{u_{01}}{Ka}\right)J_0\left(u_{01}\frac{r}{a}\right)
\end{aligned} \tag{5B}$$

Along the direction of transmission, z axis, there is no electric field component.

The dielectric constant of metal is usually higher than that of the dielectric medium. At 0.3 μm < λ < 4.0 μm, it increases with wavelength. Our calculations show that the transverse TE_{01} mode has the lowest loss in a metal waveguide. By properly choosing the radius a, TE_{01} has an attenuation constant α_{01} that is lower than that of the EH_{11} mode in a dielectric waveguide (see Figure 9 in reference 2).

II. Transmission Constant of the Waveguide Mode

When (1) and (2) are satisfied, the Eigen function of the transmission constant can be simplified as follows:

$$J_{n-1}(K_i a) = i\nu_n (K_i/K) J_n(K_i a) \tag{6}$$

With regard to a complex mode EH_{nm}, we have:

$$\nu_n = \frac{1}{2}(\nu^2+1)/\sqrt{\nu^2-1} \tag{7A}$$

Dividing both sides of equation (4) by K^2, we get:

$$(K_i/K)^2 = 1-(\gamma/K)^2 \tag{7B}$$

From (2) we know that $\gamma/K \approx 1$, then $K_i/K \approx 0$.

Therefore, the right side of equation (6) is zero. An approximation is made by using a micro-perturbation method. We get $K_i a \approx u_{nm}(1-i\nu_n/Ka)$. Thus, an expression for the transmission constant γ can be obtained. Substituting the value of K_i into equation (4), we have:

$$\gamma^2 = K^2 - \left(\frac{u_{nm}}{a}\right)^2 (1-i\nu_n/Ka)^2 \tag{7C}$$

After neglecting second-order terms, we obtain:

$$\begin{aligned}\gamma &= K\left[1-\left(\frac{u_{nm}\lambda}{2\pi a}\right)^2 (1-i\cdot\nu_n\cdot 2/Ka)\right]^{1/2} \\ &\approx K\left[1-\frac{1}{2}\left(\frac{u_{nm}\lambda}{2\pi a}\right)^2 (1-i\nu_n\lambda/\pi a)\right]\end{aligned} \tag{8}$$

The real and imaginary parts of the complex transmission constant γ are the phase constant β_{nm} and loss constant α_{nm}, respectively, of the mode. We can express these constants as:

$$\beta_{nm} = \frac{2\pi}{\lambda}\left\{1-\frac{1}{2}\left(\frac{u_{nm}\lambda}{2\pi a}\right)^2\left[1+I_m\left(\frac{\nu_n\lambda}{\pi a}\right)\right]\right\}$$

$$\alpha_{nm} = \left(\frac{u_{nm}}{2\pi}\right)^2 \frac{\lambda^2}{a^3}\,\mathrm{Re}(\nu_n) \tag{9}$$

The transmission loss of EH_{11} can be found based on equation (9) using a glass waveguide as an example. Assuming λ = 10.6 μm, a = 4 mm and using known parameters such as ν = 1.5 and u_{11} = 2.405, α_{11} can be calculated to be 9.76×10^{-4}/M. It can be converted to dB by a multiplying constant of 8.68 (i.e., 20 log E/E_o = dB = 20 log $e^{\alpha L}$ = $\alpha L \times 8.68$). Thus, we have α_{11} = 8.5×10^{-3} dB/M. This is a negligible transmission loss. Even with a low-gain single-pass FEL with a gain G = 0.037/M,[3] this transmission loss can be omitted. In reality, the FEL gain is much higher.

Equation (9) shows that the transmission loss α_{nm} for a specific mode is proportional to the square of the wavelength λ and inversely proportional to

the cube of the tube radius a. Figure 2 shows the attenuation constant of the EH_{11} mode as a function of λ/a, where λ is the variable ranging from 10^{-4} M to 10^{-7} M; $\nu = 1.5$ is the index of refraction of glass. Obviously, with the proper wavelength and radius, it is possible to obtain a low-loss EH_{11} mode.

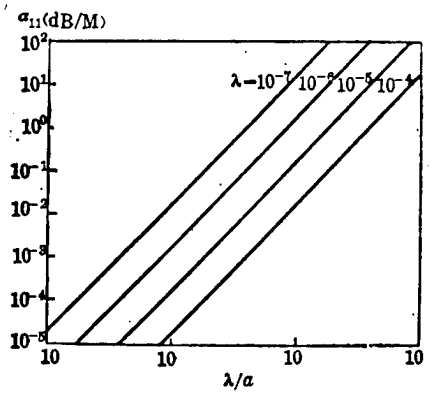

Figure 2. Attenuation of EH_{11} vs. λ/a

III. Coupling Loss of Waveguide Mode

The coupling problem involves the coupling between the transmission mode in the waveguide and the "quasi-Gaussian mode" in free space. The waveguide can be considered as a radiation source. If the equi-potential phase plane matches the reflective surface of the waveguide, then the coupling loss is minimized. At a distance z away from the waveguide, the curvature of the quasi-Gaussian wavefront can be expressed as:

$$R' = b(z/b + b/z) \tag{10}$$

where $b = \pi\omega_0^2/\lambda$ is the confocal parameter of the quasi-Gaussian light beam. When the waist radius of the quasi-Gaussian beam is $\omega_0 = 0.643a$, the coupling loss is minimal.[4] Of course, when the radius of curvature R of the reflective mirror of the waveguide cavity is identical to the wavefront, the coupling loss is the least.

J. J. Degnan discussed the coupling loss associated with finite-aperture mirrors and presented three types of low-coupling-loss cavity structures:[5] (1) large-radius-of-curvature mirror near the outlet of the waveguide, (2) large-radius-of-curvature mirror with center of curvature at the outlet of the waveguide, and (3) small-radius-of-curvature mirror with its focus at the outlet of the waveguide. The laser beam from the waveguide expands due to diffraction. If a plane mirror is used to reflect the laser beam, there is some coupling loss because it is not all collected. The coupling loss for EH_{11} is:

$$\alpha_{11}^{c} = 6.05(d/Ka^2)^{3/2} \tag{11}$$

where d is the distance between the reflective mirror and the waveguide, as shown in Figure 3. In order to minimize such losses, the mirror should be as close to the waveguide as possible. However, a certain d is required for FEL to lead the electron beam into and out of the resonance cavity. Obviously, the first type of cavity is not suitable.

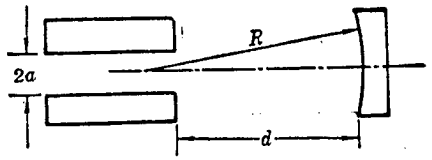

Figure 3. Position of Cylindrical Waveguide and Reflective Mirror

The second type is similar to a common center cavity used in lasers. In this case, we have:

$$z \approx R$$

The third type is similar to a confocal design. We have z ≈ R/2. The coupling loss of EH_{11} was given by Degnan as:

$$\alpha_{11}^{c} = 1 - \left[\frac{f}{2gJ_1(u_{01})}\right]^4 \left| \int_0^{h^2} d\omega_1 e^{if[(1-g)/g]\times\omega_1} \times \left[\int_0^1 d\omega_0 e^{i(f\omega_0/2g)} J_0(u_{01}\sqrt{\omega_0}) J_0\left(\frac{f}{g}\sqrt{\omega_1\omega_0}\right)\right]^2 \right|^2 \qquad (12)$$

where $f = Ka^2/R$, $g = d/R$, $h = c/a$, R is the radius of curvature of the mirror, and c is the radius of the mirror.

Let us consider the far-field condition where f/g ≈ 0 by moving the mirror in the z direction. The aperture of the mirror is so chosen that the factor fh = K ac/R is greater than or equal to the second, third and fourth root of the Bessel function $J_0(u)$. Thus, we can limit the mode to achieve the minimum coupling loss. The coupling loss is approximately 0.06 dB.

It is demonstrated that the FEL mode-transmission problem can be treated by waveguide laser theory. Transmission loss and coupling loss can be easily calculated as the basis for the design of FEL cavity resonators.

References

1. J. A. Stratton, "Electromagnetic Theory," McGraw Hill Book Co., New York and London, 1941, 524.

2. E. A. J. Marcatili, et al., BELL SYST. TECH. J., 43, pp 1783-1809, 1964.

3. Wang Mingchang, et al., GUANGXUE XUEBAO [ACTA OPTICA SINICA], 3 (9), pp 779-784, 1983.

4. R. L. Abrams, IEEE J. QUANT. ELECTR., QE-8 (9), 940, 1972.

5. J. J. Degnan, et al., IEEE J. QUANT. ELECTR., QE-9 (8), pp 901-910, 1973.

Optical Parallel Array Logic Based on Spatial Amplitude Pattern Encoding for Use in Digital Optical Computing

91FE0436A Shanghai ZHONGGUO JIGUANG [CHINESE JOURNAL OF LASERS] in Chinese Vol 18 No 1, Jan 91 pp 56-62 [MS received 28 Dec 88]

[Article by Zhong Lichen [6988 4539 2525], Zhang Ji [1728 2060], Liu Weiwei [0491 5633 5633], Guo Yili [6753 1150 3810], and Zhou Bingkun [0719 3521 3824], Department of Information Electronics, Qinghua University, Beijing: "Optical Array Logic Based on Spatial Amplitude Pattern Encoding for Use in Optical Digital Computing"]

[Text]

Abstract

The principles and characteristics of a spatial amplitude encoding pattern method for implementation of optical parallel array logic are described. A system algorithm for the design of high-speed parallel combinational operations is presented and the physical meaning of the AND and OR arrays is clarified. In addition, the results of 16 combinational logic operations in an 8f coherent optical processing system are presented.

1. Introduction

Binary logic operations, which are the basis of digital computing, are nonlinear by nature. These operations are readily performed in serial fashion by using electronic components, and as a result, serial electronic computers have achieved great success. But optical nonlinear components (such as optical bistable devices) that can perform parallel computations are still in the early laboratory stage of basic research; what kind of optical parallel logic, then, is capable of decreasing the difficulties posed by nonlinearity while thoroughly retaining the advantages of the parallel characteristics of light? The answer is, the use of coding techniques.[1] Optical parallel logic is divided into three stages: nonlinear encoding, linear logic operations, and nonlinear decoding. The difficulties associated with nonlinearity are confined to coding and decoding, and the linear logic operations can thus be carried out at nearly the speed of light. But what is the most appropriate structure for linear parallel logic? Although several suggestions have already been offered,[2,6] there is thus far no universally acceptable concept. Tanida and Ichioka's shadow-casting method offers great hope for digital optical computing and especially for optical digital image processing.

Because the method is relatively simple in structure, some promising parallel algorithms, such as optical cellular logic, optical neural-network computations, symbol replacement and the like can be performed with this type of parallel logic,[3] and it is already attracting a great deal of attention.

In the shadow-casting method, the projection is altered by changing the switching mode of an LED light source, and a fixed decoding mask is used to perform 16 parallel logic operations and spatial translation operations on two 2-dimensionally coded inputs. This is in essence a fixed spatial logic. Recently, T. Yatagai has proposed a spatial pattern encoding technique as a modification of the shadow-casting method.[4] In his spatial encoding method, parallel logic operations are implemented by changing the decoding mask rather than the switching mode of an LED, thus yielding a multiple-instruction-stream multiple-data-stream (MIMD) type of variable spatial logic. The two methods differ in structure, and the decoded output from the spatial encoding pattern method does not consist of binary values, but instead consists of two-dimensional (2D) binary spatial codes; it thus differs greatly in form from the shadow-casting method. But Yatagai does not provide any further analysis of these structural and algorithmic problems and does not implement them in an optical system. In the present paper we present a rigorous analysis of the linear parallel array logic structure of the spatial encoding pattern method and give the AND and OR array gates a more definite physical meaning. These results will be of great help in the design of gate-array hardware and in addition will lay a firm foundation for the use of the spatial encoding pattern method in the design of parallel algorithms.

2. Spatial Amplitude Pattern Encoding of Two-Valued Images or Data

In the spatial amplitude encoding pattern method, let A and B be two 2-valued input images expressed by the function $f(x, y)$, where f expresses the light intensity (i.e., amplitude) and can have only two values, 0 (black or non-transmitting) and 1 (white or transmitting). In the present paper we shall always assign white the value 1. At this stage the amplitude is digitized, but the spatial coordinates (x and y) are still continuous quantities. Spatial digitization is carried out in the coding process. The digitized space is subdivided into an array of square cells. For convenience, we assume that every cell is a square with sides of length 1; we then use a pair of integers (i, j) $(i, j = 0, 1, 2, \cdots)$ to express the address of the cell (see Figure 1). In the figure, (i, j) represents some particular cell; $(i + m, j + n)$ is another cell translated with respect to (i, j); and m and n are positive or negative integers, respectively, expressing displacements in the x and y directions that are multiples of the unit distance 1. Each pixel occupies one cell, and its intensity is expressed solely in terms of the two-valued "gray level" of the image at (i, j). A digitized image can be expressed as a matrix of pixel values (0's or 1's).

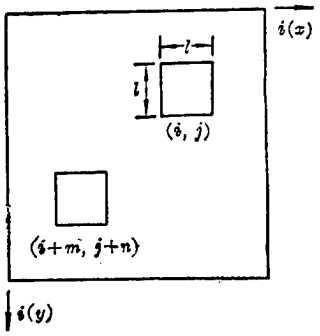

Figure 1. Pixels on 2D Digital Plane

The key to the spatial encoding pattern method is that two-valued input images A and B are represented as specified one-dimensional codes in the y and x directions, respectively. Each cell of image A or B is divided into a black-and-white pattern in the x and y directions, respectively; modulation of the pattern depends on the intensity of cell (i, j) (see Figure 2a). In this way, we arrive at a one-dimensional α-coded or β-coded pattern (see Figure 3). The intensity of every pixel (i, j) in a one-dimensionally coded pattern is replaced by a binary code α_{ij} or β_{ij}. Spatially, this code is represented by two one-dimensional modulation pulses, each consisting of a binary 0 or 1. The 0 or 1 can be expressed as a light amplitude, a direction of polarization, a phase, or a wavelength, with corresponding use of amplitude modulation, polarization modulation, phase modulation or frequency modulation. In the present paper we confine the discussion to the most basic and simplest case, that of amplitude modulation, and we do not consider optical hardware implementation. The α_{ij} or β_{ij} can be expressed by an ordered pair of binary numbers, and the most convenient method is therefore to write them as a vector. In Figure 2b, α_{ij} and β_{ij} are respectively represented as a two-element column matrix $\begin{pmatrix}\alpha_1\\ \alpha_2\end{pmatrix}$ and a two-element row matrix (β_1, β_2), in which α_1, α_2, β_1 and β_2 are binary digits (0 or 1) whose values depend on the gray levels A(i, j) or B(i, j) of images A and B at location (i, j).

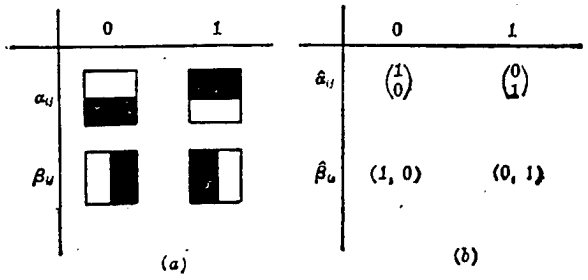

Figure 2. (a) One-Dimensional Coding Patterns of A and B;
(b) Corresponding Matrix Representations

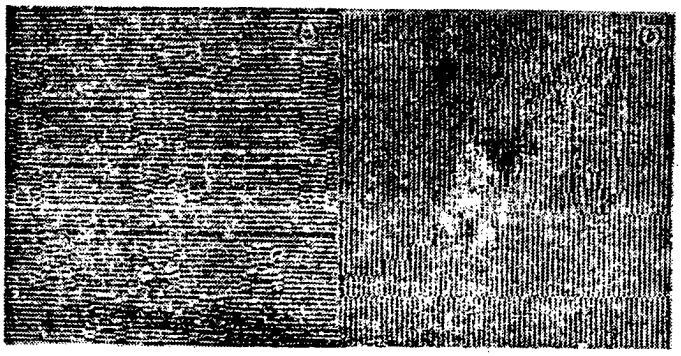

Figure 3. One-Dimensional α-Coded Pattern for A (left) and One-Dimensional β-Coded Pattern for B (right)

The present discussion of the spatial amplitude encoding pattern method deals only with amplitude modulation. Figure 3 was obtained by photoetching a 128-bit one-dimensional coding mask on a 25 x 25 mm surface. Two one-dimensional coding masks α and β are superimposed with their x and y axes orthogonal in order to obtain a 2D coding pattern θ. The superposition operation is equivalent to parallel logic multiplication of α and β. Some hardware components cannot be in direct contact during operation, and a phase multiplication technique in which they are separate is therefore convenient. In order to decrease alignment difficulties, thorough use was made of existing results in Fourier optics; the most convenient method is implemented in an 8f system as shown in Figure 4. The 8f system is a coherent optical linear processing system that is well suited to linear encoded logic processing. In addition, it has superior optical-information processing capabilities, such as convenient implementation high- and low-pass filters, bandpass filters and matching filters in the frequency-spectrum plane.

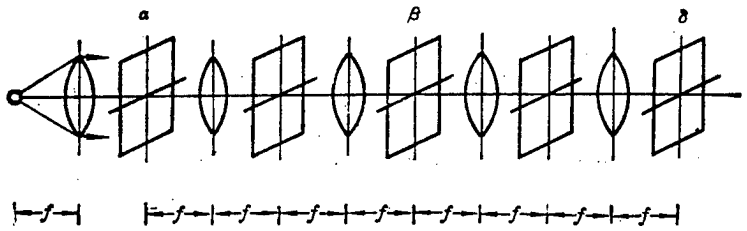

Figure 4. 8f Coherent Optical Processing System in Which Optical Parallel Array Logic Is Implemented by Means of the Spatial Amplitude Encoding Pattern Method

In Figure 5, δ is a two-dimensional decoding mask or "operation kernel mask" which stores the logic operation kernel; it has 16 two-dimensionally coded modulation modes. Each mode corresponds to a unique linear coding logic function. Every pixel (i, j) must be divided into four equal smaller squares, each of which is either black or white, thus yielding 16 modulation (encoding) modes which differ in the distribution of black and white and correspond to the 16 logic operation functions that are to be coded. We use

δ_{11}, δ_{12}, δ_{21} and δ_{22} to express the binary values of the cells, and we write the 2 x 2 binary array $\hat{\delta}_{ij}=\begin{pmatrix}\delta_{11} & \delta_{12}\\ \delta_{21} & \delta_{22}\end{pmatrix}$. Figure 5 shows the corresponding logic operation symbols and the notation for the 2 x 2 decoding array. The 2D code on decoding mask δ may be the same in every position (i.e., $\hat{\delta}_{ij}$ is constant as (i, j) changes, so that it represents fixed-spatial-logic, single-instruction-stream multiple-data-stream (SIMD) processing). If $\hat{\delta}_{ij}$ changes with (i, j), the mask represents an MIMD variable spatial logic.

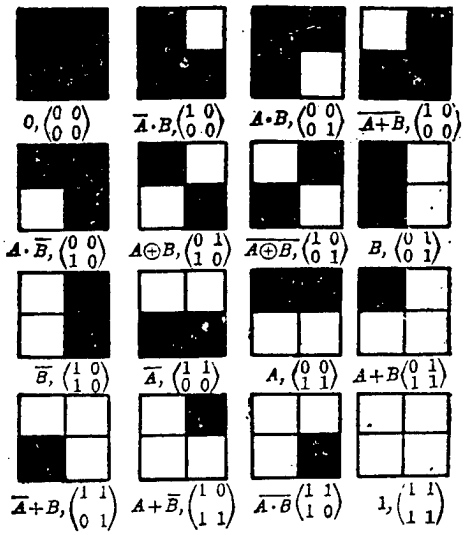

Figure 5. Sixteen 2D Codes in Decoding Mask δ

Figure 6 shows the output $\gamma(k)$ resulting from the application of the 16 linear-coded logic operations to images A and B by means of mask photoetching technology in an 8f optical system. The photograph is a two-dimensional 64 x 64 = 4096-bit digital image of 16 logic operations on a 25 x 25 mm surface. If the symbol $\wedge$ is used to express the operation of parallel superposition of the decoding mask and encoding mask, then the processing that is performed can be represented by the triple product:

$$\alpha[A(i, j)] \wedge \beta[B(i, j)] \wedge \delta(k) = \gamma(i, j, k) \qquad (1)$$

For fixed spatial logic, we require only four photoetched mask elements. In Figure 5, these are the four codes in the second column. The other 10 codes can be obtained by simple spatial translation and rotation of these four mask elements. The 0 and 1 masks can be replaced by fast optical gates. In the present paper we shall discuss only fixed spatial logic. In Figure 7, the 16 logic operations are encoded, using the simple notation k = 0, 1, 2, $\cdots$, 15.

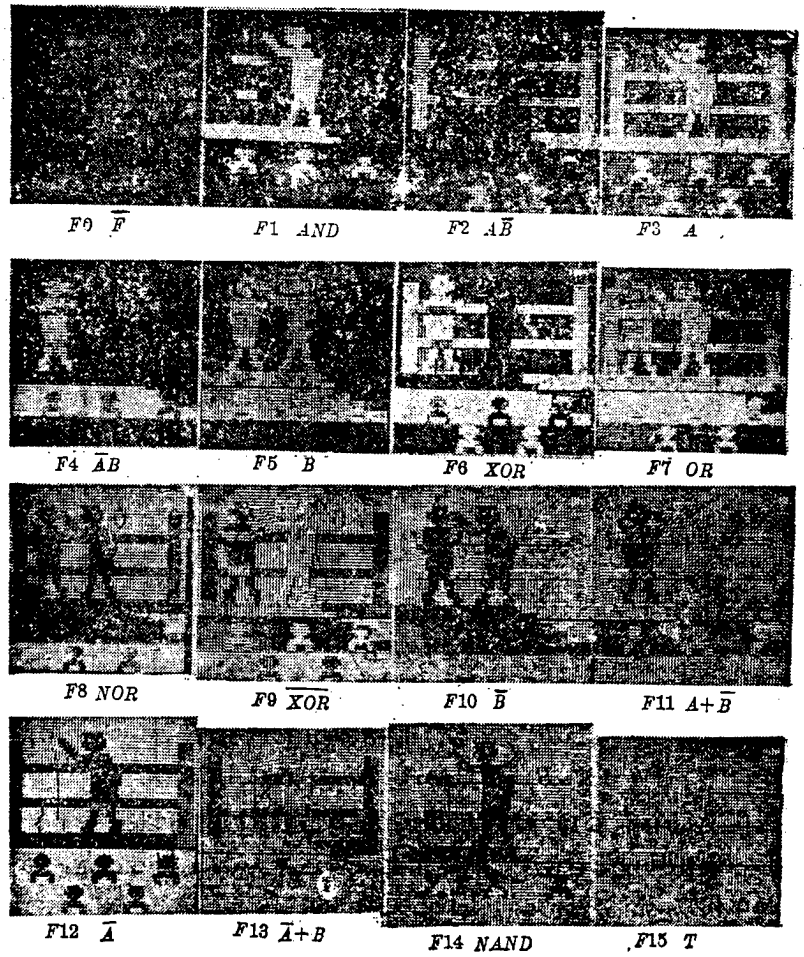

Figure 6. Experimental Results Depicting 16 Possible Functions Obtained With Optical Array [Logic] Gates of the 8f Coherent Optical Processing System

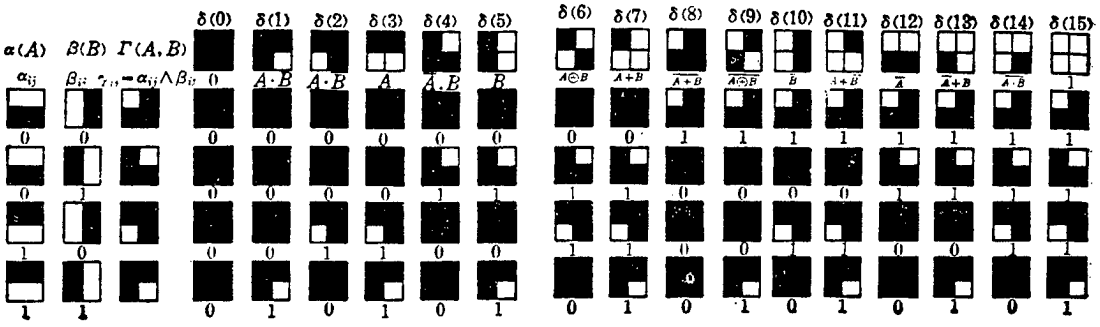

Figure 7. Optical Representations of 16 Possible Logic Function Processing Elements (i, j): 1 (white) represents true value

3. Implementation of Optical Parallel Array Logic

In the operation $\alpha \wedge \beta = \theta$, in which two one-dimensional codes are multiplied, the transmitted light intensity distribution represents the 2D code θ, in which each pixel (i, j) is replaced by four smaller black or white squares. The modulation method for this 2D code depends on the values of A(i, j) and B(i, j) and is expressed as the 2 x 2 matrix $\hat{\theta}_{ij} = \begin{pmatrix} \theta_{11} & \theta_{12} \\ \theta_{21} & \theta_{22} \end{pmatrix}$ in which θ_{11}, θ_{12}, θ_{21} and θ_{22} are all binary digits. The relationship between $\hat{\theta}_{ij}$ and $\hat{\alpha}_i = \hat{\alpha}[A(i, j)]$, $\hat{\beta}_{ij} = \hat{\beta}_{ij}[B(i, j)]$ is:

$$\hat{\theta}_{ij}(A, B) = \hat{\alpha}[A(i,j)] \otimes \hat{\beta}[B(i, j)] \tag{2}$$

where $\otimes$ denotes the outer product of the matrices. As a consequence, the operation $\alpha \wedge \beta$ can be expressed mathematically as the outer product of two one-dimensional matrices. Substituting the binary digits into equation (2), we obtain:

$$\left.\begin{aligned}
\hat{\theta}_{ij}(0, 0) &= \hat{\alpha}_{ij}(0) \otimes \hat{\beta}_{ij}(0) = \begin{pmatrix} 1 \\ 0 \end{pmatrix} (1 \quad 0) = \begin{pmatrix} 1 & 0 \\ 0 & 0 \end{pmatrix} \\
\hat{\theta}_{ij}(0, 1) &= \hat{\alpha}_{ij}(0) \otimes \hat{\beta}_{ij}(1) = \begin{pmatrix} 1 \\ 0 \end{pmatrix} (0 \quad 1) = \begin{pmatrix} 0 & 1 \\ 0 & 0 \end{pmatrix} \\
\hat{\theta}_{ij}(1, 0) &= \hat{\alpha}_{ij}(1) \otimes \hat{\beta}_{ij}(0) = \begin{pmatrix} 0 \\ 1 \end{pmatrix} (1, \ 0) = \begin{pmatrix} 0 & 0 \\ 1 & 0 \end{pmatrix} \\
\hat{\theta}_{ij}(1, 1) &= \hat{\alpha}_{ij}(1) \otimes \hat{\beta}_{ij}(1) = \begin{pmatrix} 0 \\ 1 \end{pmatrix} (0, \ 1) = \begin{pmatrix} 0 & 0 \\ 0 & 1 \end{pmatrix}
\end{aligned}\right\} \tag{3}$$

where the characteristic of matrix elements $\hat{\theta}_{ij}$(A, B) is that three of them are 0's and one of them is a 1. This characteristic is very important. We know from equation (2) that:

$$\left.\begin{aligned}
\theta_{11}(A, B) &= \alpha_1(A)\beta_1(B) \\
\theta_{21}(A, B) &= \alpha_2(A)\beta_1(B) = \alpha_1(A)\beta_1(B) \\
\theta_{12}(A, B) &= \alpha_1(A)\beta_2(B) = \alpha_1(A)\bar{\beta}_1(B) \\
\theta_{22}(A, B) &= \alpha_2(A)\beta_2(B) = \bar{\alpha}_1(A)\bar{\beta}_1(B)
\end{aligned}\right\} \tag{4}$$

In parallel array logic gates, every element (i, j) corresponds to a variety of optical processing operations. As a consequence, each element (i, j) may be regarded as a spatial processing element. Here we shall discuss only logical operations on processing elements (i, j). For simplicity of notation, we temporarily omit the subscripts i and j. In Boolean algebra, the matrix elements are clearly related as follows:

$$\left.\begin{aligned}
\bar{\alpha}_1(A) &= \alpha_2(A) = \alpha_1(\bar{A}) \\
\bar{\beta}_1(B) &= \beta_2(B) = \beta_1(\bar{B})
\end{aligned}\right\} \tag{5}$$

and we can establish the second equality in equation (4) by means of equation (5). Ultimately, the matrix elements $\hat{\theta}_{ij}(A, B)$ in equation (4) can be expressed exclusively in terms of products of $\alpha_1(A)$, $\beta_1(B)$ and their negations $\bar{\alpha}_1(A)$ and $\bar{\beta}_1(B)$.

This important result indicates that every pixel $\theta_{ij}(A, B)$ in 2D spatial code $\theta(A, B)$ is equivalent to a parallel AND logic register at processing element (i, j); this register concurrently stores four product terms, $\alpha_1(A)\beta_1(B)$, $\bar{\alpha}_1(A)\beta_1(B)$, $\alpha_1(A)\bar{\beta}_1(B)$, and $\bar{\alpha}_1(A)\bar{\beta}_1(B)$. In this sense, $\theta(A, B)$ is a parallel AND logic array gate.

If decoding mask (operation kernel mask) $\delta(k)$ and pattern $\theta(A, B)$ are superimposed, we obtain the 16-output logic function $\gamma(A, B, k)$. This operation has already been expressed in equation (1). For processing element (i, j), $\gamma_{ij}(A, B, k)$ can also be expressed as a 2 x 2 matrix:

$$\hat{\gamma}_{ij}(A, B, k) = \begin{pmatrix} \gamma_{11}(k) & \gamma_{12}(k) \\ \gamma_{12}(k) & \gamma_{22}(k) \end{pmatrix} \tag{6}$$

From the physical meaning of equation (6), it is evident that:

$$\begin{aligned} \gamma_{11}(k) &= \delta_{11}(k)\theta_{11}(A, B) = \delta_{11}(k)\alpha_1(A)\beta_1(B) \\ \gamma_{12}(k) &= \delta_{12}(k)\theta_{12}(A, B) = \delta_{12}(k)\alpha_1(A)\bar{\beta}_1(B) \\ \gamma_{21}(k) &= \delta_{21}(k)\theta_{21}(A, B) = \delta_{21}(k)\bar{\alpha}(A)\beta_1(B) \\ \gamma_{22}(k) &= \delta_{22}(k)\theta_{22}(A, B) = \delta_{22}(k)\bar{\alpha}_1(A)\bar{\beta}_1(B) \end{aligned} \tag{7}$$

As a result, pixel (i, j) of the coded output $\gamma_{ij}(A, B, k)$ is also expressed as a 2 x 2 binary matrix, and its corresponding spatial modulation is a 2D binary code. We must also provide a clear definition of the binary value $D\gamma_{ij}(A, B, k)$ corresponding to pixel (i, j). It is readily seen that of the four array elements given by equation (7) (for particular A, B, k, and (i, j)), only one array element can have a value of 1: in other words, two or more array elements cannot concurrently have the value 1. As a result, we define:

$$D\gamma_{ij}(A, B, k) \equiv 1, \quad \text{where there is a "1" element in Eq. (7)} \tag{8}$$

$$D\gamma_{ij}(A, B, k) \equiv 0, \quad \text{where all elements in Eq. (7) are "0"} \tag{9}$$

By virtue of definition (9), we now can use the four product terms given by equation (4) to expand $D\gamma_{ij}(A, B, k)$ as a linear logical sum:

$$\begin{aligned} D\gamma_{ij}(A, B, k) = {} & \delta_{11}(k)\alpha_1(A)\beta_1(B) + \delta_{12}(k)\alpha_1(A)\bar{\beta}_1(B) + \delta_{21}(k)\bar{\alpha}_1(A)\beta_1(B) \\ & + \delta_{22}(k)\bar{\alpha}_1(A)\bar{\beta}_1(B) \end{aligned} \tag{10}$$

Formula (10) has been proved correct in the formalism of array logic.[5] In other words, any logic operation on input signals a and b can be expanded as a linear logic sum of four logic product terms:

$$c=\alpha ab+\beta a\bar{b}+\gamma \bar{a}b+\delta \bar{a}\bar{b}$$

where α, β, γ and δ are all binary numbers. In the shadow-casting method, $\begin{pmatrix} \alpha & \gamma \\ \beta & \delta \end{pmatrix}$ is an operation kernel governed by the switching mode of the LED source. In the spatial encoding pattern method, it is replaced by $\begin{pmatrix} \delta_{11}(k) & \delta_{12}(k) \\ \delta_{21}(k) & \delta_{22}(k) \end{pmatrix}$. Physically, equation (10) states that the address-wise performance of operation k on the products stored in all of the processing elements of AND array gate θ(A, B) yields the OR-ing of four product terms. Equation (10) is also a direct consequence of definition (9). γ(A, B, k) is a binary digital image resulting from 2D encoding: it is a digital logical pattern resulting from a 2D encoded 1 (white) logical value on a 0 (black) logical background. γ(A, B, k) is actually an OR array gate. Equation (1) states that it can be obtained by parallel superposition of three input coding masks α(A), β(B) and δ(k). For k = 15 (where 1 represents the true case), we obtain γ(A, B, 15) = θ(A, B). Then (see function F15 in Figure 6) every array element will contain one white square and three black squares, and as a result, the binary gray level of each pixel will be a 1; in other words, $D\gamma_{ij}$(A, B, 15) $\equiv$ 1. But the position of the white square in each quadrisected pixel depends on (A, B), and thus A and B are implicitly stored.

Figure 7 shows 16 binary encoded pattern logic functions of two variables per pixel. The two columns at the extreme left express the one-dimensional code α or β for the two two-valued input variables, and the third column represents the binary code θ; the topmost row expresses the 16 2D coding operation kernels δ(k), k = 0, 1, 2, $\cdots$, 15, and the 16 rows corresponding to the δ(k) express the 16 logical outputs γ. The above reasoning can be verified by means of Figure 7.

In this paper we have given a rigorous analysis and proof of the optical parallel logic array structure of the spatial amplitude encoding pattern method, we have presented a clear physical interpretation of the parallel AND array gate θ and the parallel OR array gate γ, and we have empirically demonstrated the validity of logic based on 16 linear coding patterns for an 8f coherent optical system. In this way, we have provided the necessary basis for further investigation of the design and optical implementation of parallel algorithms. Amplitude coding is simple in theory and is easy to grasp, but the connections between levels are difficult to implement in computer system design; however, our results will point the way for the design of polarization-coded logic structures and the development of coding hardware.

The authors are most grateful to the National Natural Science Foundation [NSFC] for its assistance in this research.

References

1. A. W. Lohmann and J. Weigelt, OPT. COMMUN., Vol 54, No 2, p 81 (1985).

2. J. Tanida and Y. Ichioka, J. OPT. AM., Vol 73, p 800 (1983); APPL. OPT., Vol 20, p 1565 (1986).

3. R. A. Athale and S. H. Lee, OPT. ENG., Vol 18, p 518 (1979).

4. T. Yatagai, OPT. LETT., Vol 11, p 260 (1986); APPL. OPT., Vol 25, p 1571 (1986).

5. Y. Ichioka and J. Tanida, PROC. IEEE, Vol 72, p 1641 (1984); J. OPT. SOC. AM., Vol A2, No 8, p 1245 (1985); APPL. OPT., Vol 27, p 6926 (1988); APPL. OPT., Vol 27, p 3819 (1988).

6. A. Ahad, S. Awwal, et al., APPL. OPT., Vol 27, p 932 (1988); Y. Li, G. Echmann, et al., APPL. OPT., Vol 25, p 2036 (1968).

Model of Experimental Hybrid Fusion-Fission Reactor Displayed

91P60193 Beijing ZHONGGUO KEXUE BAO [CHINESE SCIENCE NEWS] in Chinese 24 May 91 p 2

[Untitled photoreport by Shao Xiaochuan [6730 1420 1557]; cf. earlier report in JPRS-CST-91-013, 20 Jun 91 p 29]

[Text] In the Eighth 5-Year Plan, China's scientists are investigating new sources of power such as nuclear energy and coal-fired magneto-hydrodynamic generation. The photo depicts one such project--a model of a hybrid fusion-fission reactor created by Chinese scientists and displayed at a recent "863 Plan" Exposition.

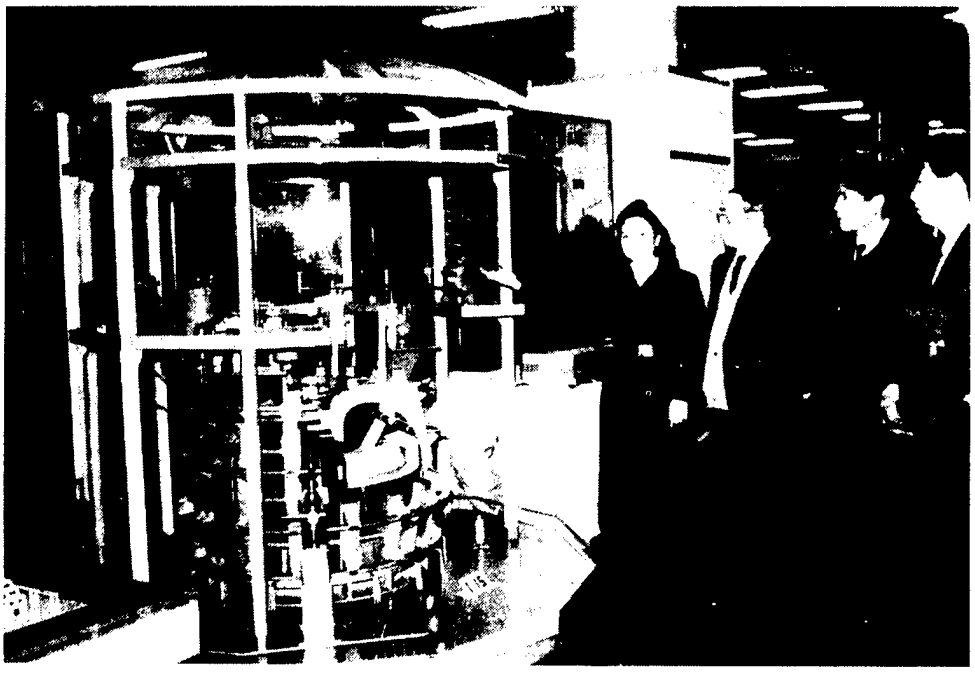

- END -

NTIS
ATTN: PROCESS 103

5285 PORT ROYAL RD
SPRINGFIELD, VA 22161

Foreign Broadcast Information Service (FBIS) and Joint Publications Research Service (JPRS) publications contain political, military, economic, environmental, and sociological news, commentary, and other information, as well as scientific and technical data and reports. All information has been obtained from foreign radio and television broadcasts, news agency transmissions, newspapers, books, and periodicals. Items generally are processed from the first or best available sources. It should not be inferred that they have been disseminated only in the medium, in the language, or to the area indicated. Items from foreign language sources are translated; those from English-language sources are transcribed. Except for excluding certain diacritics, FBIS renders personal and place-names in accordance with the romanization systems approved for U.S. Government publications by the U.S. Board of Geographic Names.

Headlines, editorial reports, and material enclosed in brackets [ ] are supplied by FBIS/JPRS. Processing indicators such as [Text] or [Excerpts] in the first line of each item indicate how the information was processed from the original. Unfamiliar names rendered phonetically are enclosed in parentheses. Words or names preceded by a question mark and enclosed in parentheses were not clear from the original source but have been supplied as appropriate to the context. Other unattributed parenthetical notes within the body of an item originate with the source. Times within items are as given by the source. Passages in boldface or italics are as published.

SUBSCRIPTION/PROCUREMENT INFORMATION

The FBIS DAILY REPORT contains current news and information and is published Monday through Friday in eight volumes: China, East Europe, Soviet Union, East Asia, Near East & South Asia, Sub-Saharan Africa, Latin America, and West Europe. Supplements to the DAILY REPORTs may also be available periodically and will be distributed to regular DAILY REPORT subscribers. JPRS publications, which include approximately 50 regional, worldwide, and topical reports, generally contain less time-sensitive information and are published periodically.

Current DAILY REPORTs and JPRS publications are listed in *Government Reports Announcements* issued semimonthly by the National Technical Information Service (NTIS), 5285 Port Royal Road, Springfield, Virginia 22161 and the *Monthly Catalog of U.S. Government Publications* issued by the Superintendent of Documents, U.S. Government Printing Office, Washington, D.C. 20402.

The public may subscribe to either hardcover or microfiche versions of the DAILY REPORTs and JPRS publications through NTIS at the above address or by calling (703) 487-4630. Subscription rates will be provided by NTIS upon request. Subscriptions are available outside the United States from NTIS or appointed foreign dealers. New subscribers should expect a 30-day delay in receipt of the first issue.

U.S. Government offices may obtain subscriptions to the DAILY REPORTs or JPRS publications (hardcover or microfiche) at no charge through their sponsoring organizations. For additional information or assistance, call FBIS, (202) 338-6735,or write to P.O. Box 2604, Washington, D.C. 20013. Department of Defense consumers are required to submit requests through appropriate command validation channels to DIA, RTS-2C, Washington, D.C. 20301. (Telephone: (202) 373-3771, Autovon: 243-3771.)

Back issues or single copies of the DAILY REPORTs and JPRS publications are not available. Both the DAILY REPORTs and the JPRS publications are on file for public reference at the Library of Congress and at many Federal Depository Libraries. Reference copies may also be seen at many public and university libraries throughout the United States.